Available online at www.sciencedirect.com
ScienceDirect
Journal of Sound and Vibration 315 (2008) 849–874
JOURNAL OF SOUND AND VIBRATION
www.elsevier.com/locate/jsvi

Acoustical response of orifices under grazing flow: Effect of boundary layer profile and edge geometry

G. Kooijman[a,*], A. Hirschberg[a], J. Golliard[b]

[a]*Fluid Dynamics Laboratory, Department of Applied Physics, Eindhoven University of Technology, P.O. Box 513, 5600 MB Eindhoven, The Netherlands*
[b]*TNO Science and Industry, P.O. Box 155, 2600 AD Delft, The Netherlands*

Received 7 February 2007; received in revised form 2 February 2008; accepted 4 February 2008
Handling Editor: C.L. Morfey
Available online 8 May 2008

Abstract

The effect of mean grazing flow on the acoustical response of a single rectangular slot in a wall to imposed sound is investigated experimentally. For this purpose an accurate multi-microphone impedance tube set-up is employed. In particular the influence of the mean grazing flow characteristics as well as the orifice's (edge) geometry is examined. For this purpose different boundary layer flows and slot geometries are used. Hot-wire boundary layer- and shear layer measurements are carried out. Care has been taken as to remain in the regime of linear acoustic perturbations. The change of the orifice's acoustic impedance due to the mean grazing flow shows an oscillating behaviour as function of the Strouhal number. It is found that, when the Strouhal number is based on the phase velocity of the spatial hydrodynamic instability of the shear layer, these oscillations coincide for different boundary layer flows. The amplitudes of the oscillations increase with decreasing laminar boundary layer thickness. The oscillations disappear when the shear layer, according to linear theory, becomes stable. Furthermore, especially the downstream edge—rather than the upstream edge—of the slot is of influence: oscillations in impedance increase up to a factor five in amplitude when the edges are sharp.

1. Introduction

The effect of grazing flow on the acoustical response of orifices has been investigated experimentally by numerous authors. Most of these studies are related to acoustic liners, which are used for sound absorption in exhaust systems of combustion engines and at jet engine inlets and outlets [1]. These liners consist of perforated plates backed with honeycomb structures, forming an array of Helmholtz resonators.

Most of the investigations therefore concentrate on the working domain of these liners, i.e. at low Strouhal numbers and boundary layers with large thickness compared to the streamwise width of the perforations. Results are often summarized in empirical laws. Generally, above a certain grazing flow velocity the resistance is found to increase improving sound absorption, whereas the reactance decreases.

*Corresponding author. Currently at: Philips Research Laboratories, High Tech Campus 36, 5656 AE Eindhoven, The Netherlands.
E-mail addresses: alohagerben@hotmail.com, gerben.kooijman@philips.com (G. Kooijman).

0022-460X/$ - see front matter © 2008 Published by Elsevier Ltd.
doi:10.1016/j.jsv.2008.02.030

Goldman and Panton [2], Kooi and Sarin [3], Goldman and Chung [4], Cummings [5] and Kirby and Cummings [6] performed experiments with circular orifices (and louvres [6]) at low Strouhal numbers. The thickness of the turbulent boundary layers they had was several times the orifice diameter. On basis of the results empirical formulae or scaling variables were given for resistance and reactance. In all cases the influence of the boundary layer is translated into a dependence on the friction velocity. In Ref. [4] it is even stated that outer boundary layer parameters, such as the boundary layer thickness, have no influence on the acoustical properties. Cummings [5] also recognized the influence of the level of boundary layer turbulence.

More recently similar experiments were done by e.g. Dickey and Selamet [7], Malmary and Carbonne [8], Lee and Ih [9] and Leroux [10]. In Ref. [7] the use of a single set of empirical expressions for different (types of) perforates was strongly questioned. Malmary and Carbonne [8] compared their results with the empirical model given by Kirby and Cummings [6]. They found it to be valid up to a Mach number of 0.6, although it originally was derived for Mach numbers up to 0.2. They also showed the discrepancy between different empirical models from literature (among which those in Refs. [3,5,6]). It was discussed that this discrepancy, besides the fact that some models do not consider boundary layer characteristics, are due to differences in experimental techniques and geometries used. Lee and Ih [9] presented an empirical model based on their experiments, which was argued to yield a better prediction of orifice impedance than models from literature. However, surprisingly they did not address the influence of boundary layer characteristics. Leroux [10] investigated the wave propagation in lined ducts with flow. Results were compared to a theoretical multimodal method, see also, e.g. Kooijman et al. [11].

In the present paper we focus on the acoustical behaviour of orifices in case the boundary layer is thin compared to the streamwise width. Experimental studies for this case are also available in literature. Ronneberger [12] measured the effect of grazing flow on the impedance of circular and oblong orifices. The boundary layer thickness, although not measured, was small (in the order of 1% of the aperture radius). He proposed an analytical model with 'considerable simplifications', which however qualitatively predicted his experimental results well. Furthermore he reasoned that boundary layer characteristics must have influence, and limited the validity of his model to the regime of small boundary layer thickness compared to orifice dimensions. In a later paper [13] Ronneberger questions his model more, especially in the higher Strouhal number range.

Golliard [14] performed experiments with rectangular slots in a 2 microphone impedance tube set up. Measurements were done for different turbulent boundary layers, with thickness in the order of the slot width L in streamwise direction, up to Strouhal numbers of order 10. He compared his results with the predictions of the analytical model for uniform grazing flow by Howe [15], which assumes an infinitely thin boundary layer and shear layer. The acoustic impedance of the orifice was expressed in terms of a non-dimensional scaled resistance $\tilde{r}_{\mathrm{flow}}$ and -reactance $\tilde{\delta}_{\mathrm{flow}}$ due to the grazing flow. These parameters will be defined below. Fig. 1 shows a fit of the results for the non-dimensional scaled resistance $\tilde{r}_{\mathrm{flow}}$ and -reactance $\tilde{\delta}_{\mathrm{flow}}$ against Strouhal number $\omega L/U_0$ for two boundary layer cases as obtained by Golliard. Here U_0 is the grazing flow velocity

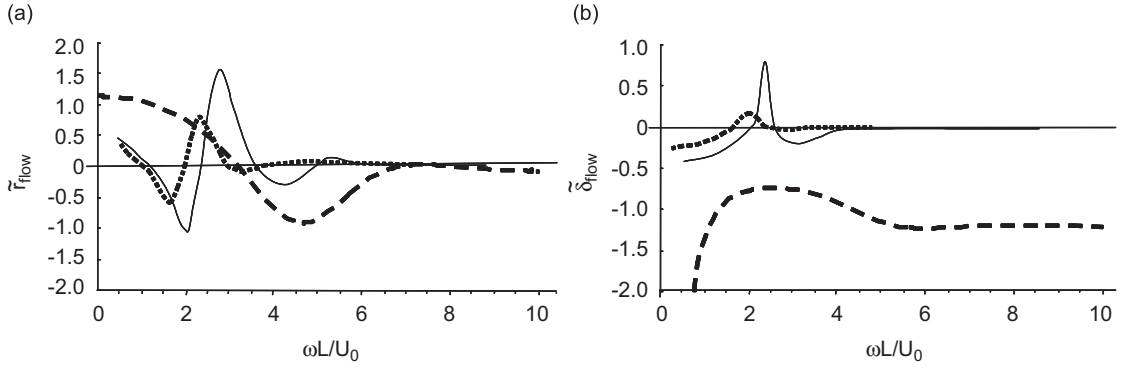

Fig. 1. Fit of the experimental results obtained by Golliard [14] for the non-dimensional scaled resistance $\tilde{r}_{\mathrm{flow}}$ (a) and reactance $\tilde{\delta}_{\mathrm{flow}}$ (b) versus Strouhal number $\omega L/U_0$ in case of a turbulent boundary layer with momentum thickness to slit width ratio $\theta/L = 0.079$ (solid line) and $\theta/L = 0.29$ (dotted line), respectively. Also the theoretical prediction of Howe [15], for one-sided grazing flow is shown (dashed line).

outside the boundary layer, and ω is the angular frequency of the sound. The boundary layer momentum thickness θ, cf. Eq. (15) further on, was 1.1 and 4.0 mm, respectively. The aperture width was $L = 1.4$ cm in flow direction and 10 cm perpendicular to the flow. The results are compared with Howe's theoretical model [15] for single-sided grazing flow. Clearly an effect of the boundary layer thickness is seen. Comparing experimental results with theory, some qualitative agreement for the resistance is found, in the sense that both show oscillating behaviour (alternate regions of positive and negative resistance). However the scaling with Strouhal number is different, an effect which is also seen when comparing the two different boundary layer cases. Furthermore, the number of oscillations in the theoretical prediction is less than in the experiments. Comparing experiment and theory for the reactance, no agreement is found. Especially, the fact that for large Strouhal number the predicted reactance $\tilde{\delta}_{\text{flow}}$ does not tend to zero is peculiar.

Considering the convection velocity of vorticity U_c as the relevant velocity for the influence of the grazing flow on impedance, subsequently a Strouhal number based on this convection velocity was employed. The convection velocity was actually chosen for each configuration such that comparison between experiment and theory was best. From this it appeared that the relation $U_c/U_0 = 0.4(\delta_{\text{tu}}/L)^{-0.2}$ provided a reasonably good fit, where δ_{tu} is the turbulent boundary layer thickness, see also Section 5.1 below. The results for the same boundary layer cases as above, cf. Fig. 1, are shown in Fig. 2. The figure also shows the theoretical result for two-sided grazing flow, where the ratio of flow velocity beneath and above the orifice equals $U_-/U_+ = 0.2$, with $U_+ = U_0$. Compared to one-sided grazing flow more oscillations are seen, giving a better (qualitative) agreement with experiments. Golliard therefore suggests that the velocity beneath the orifice, induced by entrainment, should be taken into account when analysing the behaviour of an orifice with one-sided imposed grazing flow. The experimental results of Golliard were first tentatively confirmed by Kooijman et al. [16]. Here, the change in orifice impedance due to grazing flow over a rectangular slot of a damped Helmholtz resonator was determined by measuring the transfer of sound from a loudspeaker outside the resonator to a microphone placed inside the resonator.

Peat et al. [17] compared measurements on circular orifices both with Howe's theory in its original form and with a modified form as proposed by Xiaodong Jing et al. [18]. Regarding the original formulation of the theory basically the same conclusions were drawn as in Golliard's work [14]. The reactance predicted by the modified theory was argued to yield better (qualitative) agreement with experimental results, whereas resistance prediction became worse. Especially negative resistance, found in some Strouhal ranges, was not predicted anymore. Furthermore, the vorticity convection velocity was not considered as the relevant velocity in comparing experiments with the modified theory, as opposed to comparison with the theory in the original formulation.

In the present paper the effect of grazing flow on the impedance of rectangular orifices is experimentally investigated by means of a multi-microphone impedance tube set-up. The aim is to provide accurate

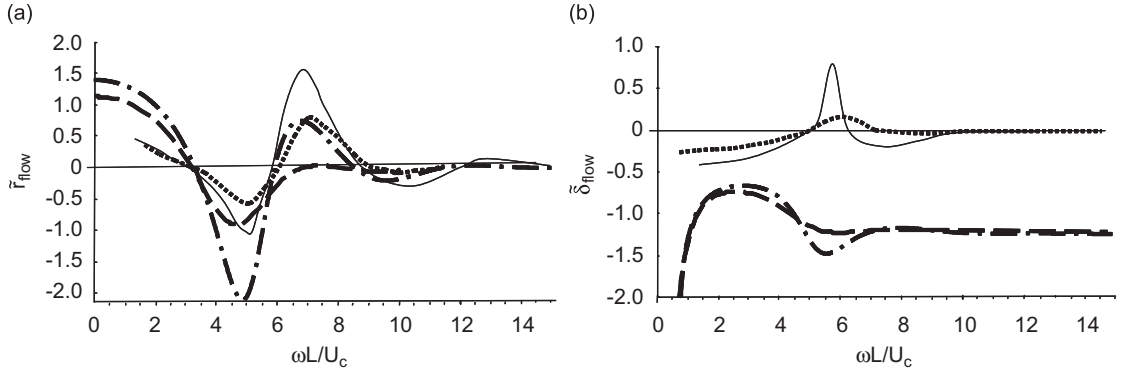

Fig. 2. Fit of the experimental results obtained by Golliard [14] for the non-dimensional scaled resistance $\tilde{r}_{\text{flow}}$ (a) and reactance $\tilde{\delta}_{\text{flow}}$ (b) in case of a turbulent boundary layer with momentum thickness to slit width ratio $\theta/L = 0.079$ (solid line) and $\theta/L = 0.29$ (dotted line), respectively. Here the Strouhal number $\omega L/U_c$ is based on the convection velocity of vorticity in the aperture. Also the theoretical prediction of Howe [15] for one-sided grazing flow (dashed line), as well as for a two sided grazing flow with ratio of flow velocity beneath and above the orifice equal to $U_-/U_+ = 0.2$ (dot-dash line) is shown.

experimental data obtained under well-defined circumstances. In this context the influence of the boundary layer characteristics of the grazing flow is examined. Furthermore, linearity and the influence of the edge geometry of the orifices—not explicitly taken into account in existing models, like that of Howe [15]—is dealt with. In the following, first the used quantities to describe the effect of grazing flow on orifice impedance will be discussed. Subsequently, the experimental set-up and the employed orifice geometries are treated. Next, a thorough characterization of the mean flow properties is given. Finally, results are presented and conclusions are drawn.

2. Quantities for the acoustical behaviour of an orifice

The acoustical behaviour of an orifice in a wall can be quantitatively expressed in several ways. The different definitions will be treated below. Furthermore, quantities to describe the effect of grazing flow on the acoustical behaviour of an orifice are given.

Consider an aperture with uniform imposed (Fourier transformed) acoustic pressure disturbances p_+ and p_- above and below, respectively. The area averaged velocity disturbance through the orifice, perpendicular to the wall, is denoted u_h.

Employing an $e^{+i\omega t}$ convention for harmonic disturbances, the Rayleigh conductivity of the aperture can be written as:

$$K_R = i\omega\rho_0 \frac{u_h S_0}{p_- - p_+}, \tag{1}$$

where S_0 is the aperture area and ρ_0 is the mass density.

Another quantity to express the acoustic properties of an orifice is the effective length l_{eff}. The approach here is that the complex flow in the orifice region can be represented by an equivalent length of the mass of fluid, with volume $S_0 l_{\text{eff}}$, which effectively participates in the acoustic motion. The effective length is found by integration of the linearized Euler equation for momentum in the direction perpendicular to the wall in which the orifice is placed:

$$l_{\text{eff}} = \frac{1}{i\omega\rho_0} \frac{p_- - p_+}{u_h} = \frac{S_0}{K_R}. \tag{2}$$

In case the motion is purely reactive, the effective length is real. If also dissipation is present, the effective length will have an imaginary part.

The last—and probably most commonly used—quantity to be discussed here, which represents the acoustical behaviour of an orifice, is the (acoustical) impedance. Non-dimensionalized to the characteristic impedance $\rho_0 c_0$ of the fluid, with c_0 the sound velocity, it is given by:

$$Z_h \equiv \frac{1}{\rho_0 c_0} \frac{p_- - p_+}{u_h} = ik_0 \frac{S_0}{K_R} = ik_0 l_{\text{eff}} \tag{3}$$

with $k_0 = \omega/c_0$. The impedance can be decomposed in a resistance r and a reactance δ:

$$r = \text{Re}(Z_h),$$

$$\delta = \frac{1}{k_0} \text{Im}(Z_h). \tag{4}$$

From Eq. (3) it follows that $\delta = \text{Re}(l_{\text{eff}})$, so that indeed δ represents the inertia of the fluid in motion in the aperture. Often the wall thickness of the aperture is subtracted from δ to obtain a quantity referred to as the end correction. Writing the resistance and reactance as function of the Rayleigh conductivity, using Eqs. (3) and (4), results in:

$$r = -k_0 \,\text{Im}\left(\frac{S_0}{K_R}\right),$$

$$\delta = \mathrm{Re}\left(\frac{S_0}{K_R}\right). \tag{5}$$

Substituting the Rayleigh conductivity for a rectangular slot with uniform grazing flow $U = U_+$ above and U_- beneath the orifice as calculated by Howe [15] gives:

$$r = -\frac{k_0 L}{\pi}\,\mathrm{Im}(2F(Sr_L,\mu) + \Psi),$$

$$\delta = \frac{L}{\pi}\,\mathrm{Re}(2F(Sr_L,\mu) + \Psi),$$

where $F(Sr_L,\mu)$ is a complex function depending on the Strouhal number $Sr_L = \omega L/U_0$ and the ratio μ of mean flow velocity beneath and above the orifice: $\mu = U_-/U_+$. The quantity Ψ is related to the local approximations of the Green function on either side of the aperture. It is determined by the geometry surrounding the aperture, and hence does not dependent on the mean flow. On basis of this result Golliard [14] proposed to subtract the resistance and reactance, respectively, without flow, such that for fixed μ:

$$r_{\mathrm{flow}} = r - r_{U=0} = -\frac{2k_0 L}{\pi}\,\mathrm{Im}(F(Sr_L) - F_{U=0}),$$

$$\delta_{\mathrm{flow}} = \delta - \delta_{U=0} = \frac{2L}{\pi}\,\mathrm{Re}(F(Sr_L) - F_{U=0}).$$

Here, $F_{U=0}$ is the value of function F in case mean grazing flow velocity is zero. Note that $F_{U=0}$ differs from the value of $F(Sr_L,\mu)$ obtained for $Sr_L \to \infty$: $F_{U=0} = 0$, whereas $F(Sr_L,\mu)|_{Sr_L\to\infty} = -2$. Subsequently, dividing r_{flow} and δ_{flow} by the Mach number $M = U/c_0$ and the slit width L, respectively, gives the non-dimensional scaled resistance and reactance due to the flow:

$$\tilde{r}_{\mathrm{flow}} = \frac{r_{\mathrm{flow}}}{M} = -\frac{2Sr_L}{\pi}\,\mathrm{Im}(F(Sr_L) - F_{U=0}),$$

$$\tilde{\delta}_{\mathrm{flow}} = \frac{\delta_{\mathrm{flow}}}{L} = \frac{2}{\pi}\,\mathrm{Re}(F(Sr_L) - F_{U=0}).$$

According to the theory of Howe [15], these quantities thus solely depend on the Strouhal number and are independent of the geometry surrounding the orifice.

Following the derivation above, in terms of the impedance the non-dimensional scaled resistance and reactance due to the flow are given by:

$$\tilde{r}_{\mathrm{flow}} = \frac{1}{M}(\mathrm{Re}(Z_h) - \mathrm{Re}(Z_{h,U=0})),$$

$$\tilde{\delta}_{\mathrm{flow}} = \frac{1}{k_0 L}(\mathrm{Im}(Z_h) - \mathrm{Im}(Z_{h,U=0})). \tag{6}$$

The acoustic pressure above the orifice p_+ equals the radiation pressure p_{rad}, which is determined by the wave equation for the medium above the orifice. Since in the presence of grazing flow the convective wave equation holds, instead of the wave equation for a medium at rest, the radiation pressure is modified by the flow. However, Ingard and Singal [19] showed that for the radiation of a piston in a moving medium this effect is very small for Mach numbers below 0.2, see also Ref. [14]. Therefore, we consider the radiation pressure to be independent of the flow. In calculating the non-dimensional scaled resistance and reactance just as well a 'one-sided' orifice impedance Z_{h-} can then be used:

$$Z_{h-} = \frac{1}{\rho_0 c_0}\frac{p_-}{u_h},$$

$$\tilde{r}_{\mathrm{flow}} = \frac{1}{M}(\mathrm{Re}(Z_{h-}) - \mathrm{Re}(Z_{h-,U=0})),$$

$$\tilde{\delta}_{\text{flow}} = \frac{1}{k_0 L}(\text{Im}(Z_{h-}) - \text{Im}(Z_{h-,U=0})). \tag{7}$$

In the following these quantities will generally be called resistance and reactance for convenience. From the context it will be clear that actually the scaled versions $\tilde{r}_{\text{flow}}$ and $\tilde{\delta}_{\text{flow}}$ are meant.

3. Impedance tube experiment

3.1. Set-up

Acoustic measurements have been performed with an impedance tube placed in a semi-anechoic room. A multi-microphone layout is chosen in order to have better accuracy in a relatively wide frequency range compared to a 'standard' 2 microphone impedance tube set-up [20–23]. Fig. 3 shows a schematic layout of the set-up. It consists of a 70 cm long smooth steel tube with an inner radius of $R = 3.5$ cm and an outer radius of 5.5 cm. A total of 7 microphones (PCB 116A) connected to charge amplifiers (Kistler 5011) are mounted in adapters in the wall of the tube. A signal generator (NI PXI-5411 arbitrary waveform generator) sends a harmonic signal with angular frequency ω via an amplifier (Toellner TOE 7608) to the loudspeaker. The loudspeaker couples the sound into the impedance tube at the back end through a piece of porous acoustical damping material. The damping material serves to prevent unwanted high acoustic amplitudes due to resonance. A plate with a rectangular slit is attached to the other end of the tube. The plate is positioned such that the orifice is centred above the tube. The geometries of the different slits used are given further on. The plate is also fixed to the nozzle of an open silent windtunnel, which generates the grazing flow over the slit. In order to prevent acoustical leaks, o-rings are placed between the microphone adapters and the tube, as well as between the plate and the tube. The signals of the microphone's charge amplifiers as well as the function generator signal are digitally sampled by a 8 channel dynamic signal acquisition (DSA) card (NI PXI-4472) at 10 kS/s. Both the DSA card and the signal generator module are driven by an embedded controller (NI PXI-8176), the three units are housed in a NI PXI-1042 8-slot chassis. For a single measurement microphone signals are recorded over a period of 100 s. Subsequently, as post-processing, lock-in amplification is performed on an integer number of signal periods to determine the complex amplitudes of the microphone signals. From this the reflection coefficient at the end plate is calculated as described below.

3.2. Impedance measurement

Below the cut-on frequency of the first higher order acoustic mode in the tube (at $f = 2870$ Hz), the acoustic pressure and velocity disturbance, p resp. u, in the tube are plane waves. The complex amplitudes are given by:

$$p(x) = p^+ \exp(-\text{i}k^+ x) + p^- \exp(\text{i}k^- x), \tag{8}$$

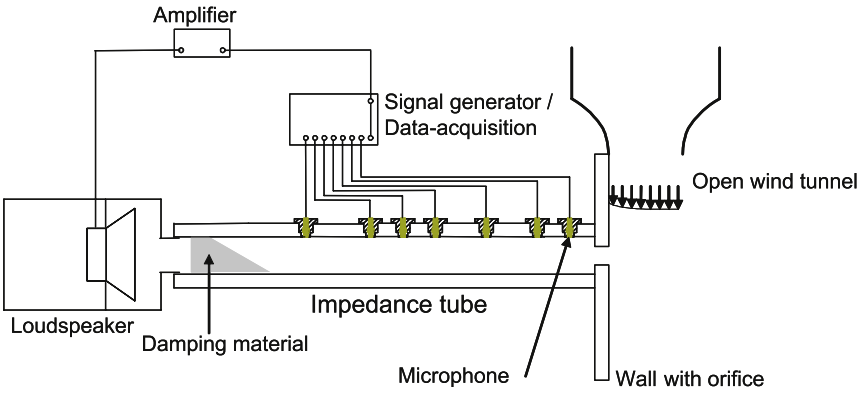

Fig. 3. Schematic layout of the impedance tube set-up.

$$u(x) = \frac{1}{\rho_0 c_0}(p^+ \exp(-\mathrm{i}k^+ x) - p^- \exp(\mathrm{i}k^- x)). \tag{9}$$

Here $p^\pm$ is the complex amplitude at $x = 0$ of the plane pressure wave travelling in positive resp. negative x-direction, i.e. to the right and to the left in Fig. 3. In case of no mean flow through the tube the wavenumber $k^\pm$ is equal in both directions. Accounting for visco-thermal damping at the walls of the tube of the acoustical waves it is given by:

$$k^\pm = \frac{\omega}{c_0}\left(1 + \frac{1-\mathrm{i}}{\sqrt{2}}\frac{1}{Sh}\left(1 + \frac{\gamma-1}{\sqrt{Pr}}\right) - \frac{\mathrm{i}}{Sh^2}\left(1 + \frac{\gamma-1}{\sqrt{Pr}} - \frac{1}{2}\gamma\frac{\gamma-1}{Pr}\right)\right) \tag{10}$$

in the low frequency approximation, $kR \ll 1$, and for high shear numbers, $Sh = R\sqrt{\omega/\nu} \gg 1$, see e.g. Peters [24]. Here ν is the kinematic viscosity, γ the ratio of specific heats at constant pressure and constant volume, and Pr is the Prandtl number. We used the properties of dry air at 20 °C and atmospheric pressure: $c_0 = 344\,\mathrm{ms}^{-1}$, $\nu = 1.51 \times 10^{-5}\,\mathrm{m}^2\,\mathrm{s}^{-1}$, $\gamma = 1.4$, $Pr = 0.71$. In the current experiments $0.03 < kR < 0.6$, and the shear number ranges from $Sh \simeq 160$ for low frequency to $Sh \simeq 700$ for high frequency. The first correction to ω/c_0, which is proportional to Sh^{-1}, affects both phase velocity and damping of the acoustic plane waves. Here, it is in the order of 2×10^{-3} (for low frequency) to 4×10^{-4} (for high frequency). The second term, proportional to Sh^{-2}, only affects the damping. In our experiments it is in the order of 10^{-3} to 7×10^{-3} of the value of the first correction for high and low frequency respectively, and therefore negligible. The effect on the damping coefficient of the plane waves due to visco-thermal losses in the bulk, see for instance Pierce [25] and Peters [24], appears to be at least two orders of magnitude smaller than that due to the losses at the wall given above. Therefore, it is neglected here. Eq. (8) can be written for all positions $x_1 \ldots x_7$ of the 7 microphones,giving an overdetermined problem for p^+ and p^-:

$$\underbrace{\begin{bmatrix} p(x_1) \\ \vdots \\ p(x_7) \end{bmatrix}}_{\mathbf{p}_m} = \underbrace{\begin{bmatrix} \exp(-\mathrm{i}k^+ x_1) & \exp(\mathrm{i}k^- x_1) \\ \vdots & \vdots \\ \exp(-\mathrm{i}k^+ x_7) & \exp(\mathrm{i}k^- x_7) \end{bmatrix}}_{\mathbf{M}_{\exp}} \begin{bmatrix} p^+ \\ p^- \end{bmatrix}. \tag{11}$$

Here we take $x = 0$ for the position of the end plate wall at the inside of the tube. The microphone positions are: $x_1 = -20\,\mathrm{mm}$, $x_2 = -70\,\mathrm{mm}$, $x_3 = -170\,\mathrm{mm}$, $x_4 = -310\,\mathrm{mm}$, $x_5 = -365\,\mathrm{mm}$, $x_6 = -410\,\mathrm{mm}$, $x_7 = -565\,\mathrm{mm}$. The overdetermined system of Eqs. (11) is solved in a least square way [26]. The solution is found by:

$$\begin{bmatrix} p^+ \\ p^- \end{bmatrix} = (\mathbf{M}_{\exp}^{\mathrm{T}}\mathbf{M}_{\exp})^{-1}\mathbf{M}_{\exp}^{\mathrm{T}} \cdot \mathbf{p}_m, \tag{12}$$

where superscript T indicates the complex conjugate transpose. The impedance Z_{h-} of the orifice, as defined in Eq. (7), is now given by:

$$Z_{h-} = \frac{1}{\rho_0 c_0}\frac{p(0)}{u_h} = \frac{S_0}{S_{\mathrm{tube}}}\frac{p^+ + p^-}{p^+ - p^-} \tag{13}$$

using Eqs. (8) and (9). Here, from conservation of mass, the acoustic velocity through the orifice, u_h, equals S_{tube}/S_0 times the acoustic velocity in the tube at $x = 0$, $u(0)$. S_0 and S_{tube} are the (cross sectional) areas of the orifice and tube, respectively. Note that in calculating the impedance by Eq. (13) the effect of visco-thermal damping on the wavenumber is not included, since it is only a small correction in the order of 10^{-3} at maximum. However, in calculating the complex pressure amplitudes $p^\pm$, cf. Eqs. (11) and (12), it is included, since it has a cumulative effect in the wave propagation.

Note that for a more conventional two microphone set-up the measurement error becomes very large if the distance between the two microphones is an integer times a half-wavelength [20,21]. Since in the present experiments 7 irregularly placed microphones are used, at most one microphone will be at (an integer times)

half a wavelength from another microphone for any frequency. This enables accurate measurements in a wide frequency range. The measurement accuracy of the set-up is assessed in the following.

3.3. Accuracy

In order to increase accuracy the microphones are calibrated with respect to a reference microphone. This is done by placing the reference microphone and the microphone to be calibrated in a closed end wall at the end of the impedance tube. In this way the same sound pressure is imposed on the microphones. Any difference in the measured complex amplitudes of the microphones results in a calibration factor. The calibration is done at several frequencies. In the subsequent acoustical measurements the reference microphone is placed at the position closest to the end wall. After calibration, the reflection coefficient $R_0 = p_-/p_+$ at a closed end wall is measured in order to assess the accuracy of the measurement set-up. Fig. 4 shows the deviation of the absolute value $|R_0|$ from unity as well as the (deviation of the) phase ϕ of the reflection coefficient scaled to 2π radians. Both are $O(10^{-3})$ (for frequencies up to 800 Hz). Note that this is a systematic error. The reproducibility of the measurement (random error) is observed to be $O(10^{-4})$. From these results the error in the measured non-dimensional scaled resistance and reactance is estimated to be in the order of 10^{-2}.

4. Orifice geometries

Measurements are done with different rectangular orifices. Schematic cross sections are given in Fig. 5. All slits are symmetrically positioned in a 1.5 cm thick 20 cm × 20 cm aluminum plate. Four slits have width $L = 1$ cm in flow direction and measure 5 cm perpendicular to the flow, cf. Fig. 5a–d. The first one has 27° sharp edges both upstream and downstream. The second one, Fig. 5b, has a single sharp 27° edge and a normal 90° edge. By rotating the plate half a turn the sharp or normal edge can be positioned upstream or downstream. The third orifice geometry, Fig. 5c, has a normal 90° edge on one side. At the other side a 0.1 mm thin phosphor bronze plate juts out 2 mm into the 12 mm wide slit in the plate, giving a sharp "0°" edge. Also here, both edges can be positioned either upstream or downstream. The last 1 cm wide slit, Fig. 5d, has two normal 90° edges. The distance of the windtunnel outlet to the upstream edge is $L_w = 9.5$ cm for these four $L = 1$ cm orifices. By rotating the plate with the orifice given in Fig. 5d a quarter turn a slit with normal 90° edges upstream and downstream is obtained measuring $L = 5$ cm in flow direction and measuring 1 cm perpendicular to the flow, cf. Fig. 5e. Distance from windtunnel outlet to upstream edge is $L_w = 7.5$ cm for this case.

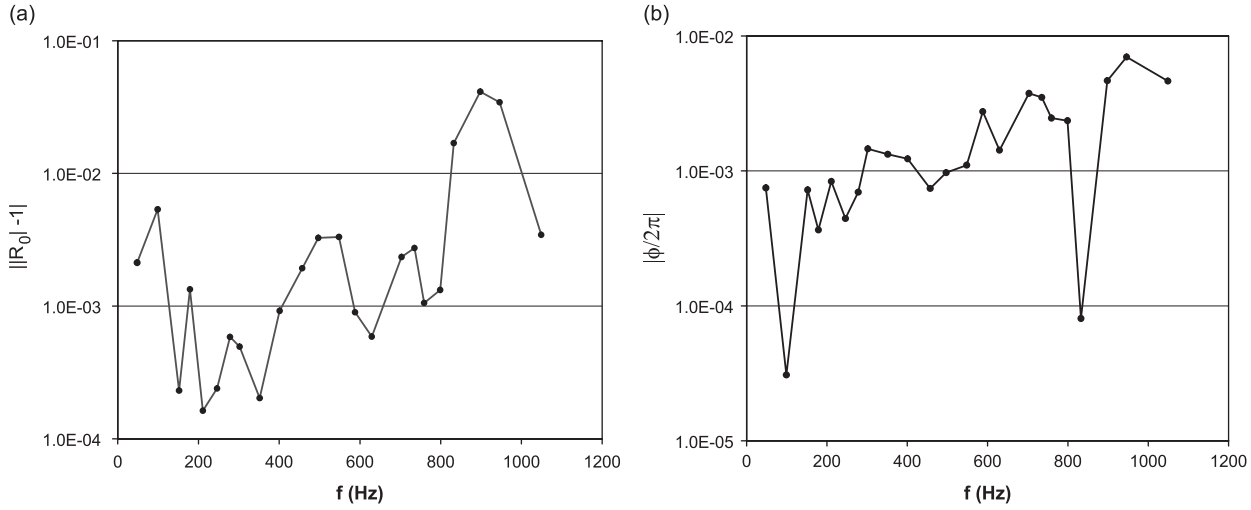

Fig. 4. Impedance tube measurements of the reflection coefficient R_0 at a closed end wall. Absolute deviation of $|R_0|$ from unity (a) and absolute value of the phase ϕ of R_0 scaled to 2π radians (b).

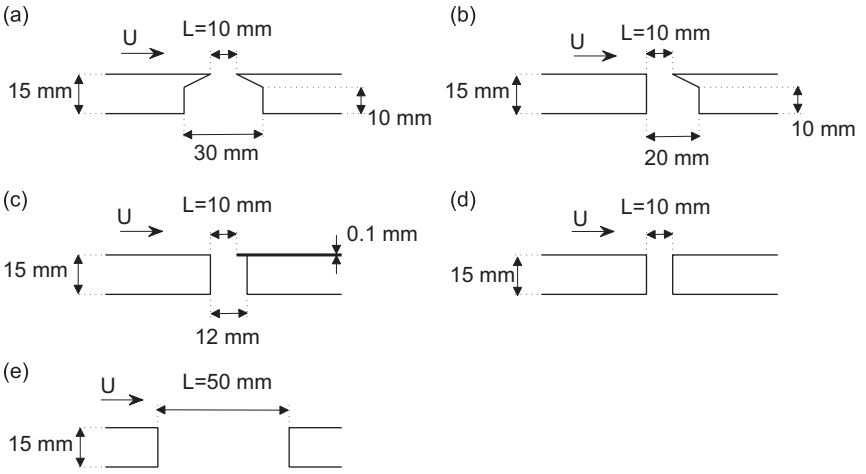

Fig. 5. Schematical cross section of the different rectangular orifices used in experiments. Slits (a)–(d) measure $L = 1$ cm in grazing mean flow direction, have width of 5 cm perpendicular to the flow, and differ in edge geometry: (a) sharp 27° edges both sides; (b) sharp 27° edge upstream or downstream; (c) sharp '0° edge' upstream or downstream; (d) 90° edges both sides. Asymmetrical slits (b) and (c) can be placed with their sharp edge either downstream (as drawn) or upstream. Slit (e) has width $L = 5$ cm in flow direction and measures 1 cm perpendicular to the flow, edges are 90° at both sides.

Table 1
Characteristics of the different boundary layers measured

Boundary layer	L_w (cm)	U_0 (m/s)	Re_{L_w}	Tripping	δ_{99} (mm)	δ_1 (mm)	θ_0 (mm)	u_{fric}/U_0	Classification
I	9.5	4.0	2.53×10^4	–	5.0	1.38	0.55		Laminar
II	9.5	6.0	3.80×10^4	–	3.8	1.10	0.46		Laminar
III	9.5	8.8	5.57×10^4	–	3.1	0.90	0.38		Laminar
IV	9.5	16.8	1.06×10^5	–	2.5	0.67	0.29		Transitional
V	9.5	16.8	1.06×10^5	Sandpaper	7.2	1.16	0.83	0.048	Turbulent
VI	9.5	16.8	1.06×10^5	Spoiler	22.4	8.80	3.90	0.0175	Turbulent wake
VII	9.5	34.1	2.16×10^5	Sandpaper	7.3	1.16	0.81	0.044	Turbulent
VIII	7.5	16.8	8.40×10^4	–	2.5	0.64	0.29		Transitional
IX	7.5	16.8	8.40×10^4	Sandpaper	7.2	1.18	0.81	0.048	Turbulent
X	7.5	16.8	8.40×10^4	Spoiler	22.3	9.13	3.63	0.0135	Turbulent wake

5. Mean flow properties

5.1. Boundary layer characterization

In order to investigate the influence of boundary layer characteristics on the effect of grazing flow on orifice impedance, different boundary layer flows—both laminar and turbulent—have been employed. The different boundary layers have been realized by varying the main flow velocity U_0 outside the boundary layer and by tripping the flow at the windtunnel outlet. For this purpose a strip of sandpaper or a spoiler are used. Detailed measurements of the boundary layer at the upstream edge of the wall aperture have been performed. For this purpose a 5 μm hot-wire is used (Dantec 55P11 on a Dantec 55H20 support connected to Streamline cta module 90C10). The hot-wire measurements are done at a sample rate of 4000 S/s for 10 s. Furthermore, measurements are done at distance $L_w = 7.5$ cm and $L_w = 9.5$ cm from the windtunnel outlet, corresponding to the different positions of the upstream edge of the wall aperture configurations used, cf. Fig. 5. The characteristics of the boundary layers based on the hot-wire measurements are listed in Table 1. A classification is also given, which will be further explained in the following.

Here $Re_{L_w} = U_0 L_w/\nu$ is the Reynolds number on the windtunnel outlet to orifice distance L_w, δ_{99} is the boundary layer thickness, where $U(\delta_{99})/U_0 = 0.99$, δ_1 is the displacement thickness:

$$\delta_1 = \int_0^\infty \left(1 - \frac{U(y)}{U_0}\right) \mathrm{d}y \tag{14}$$

and θ_0 is the momentum thickness of the boundary layer:

$$\theta_0 = \int_0^\infty \frac{U(y)}{U_0}\left(1 - \frac{U(y)}{U_0}\right) \mathrm{d}y. \tag{15}$$

It was found that the profiles for $L_w = 7.5\,\mathrm{cm}$ are almost similar to the equivalent profiles at $L_w = 9.5\,\mathrm{cm}$. The largest difference here is seen for the spoiler-tripped boundary layer. Also, the sandpaper-tripped boundary layers with $U_0 = 16.8\,\mathrm{m/s}$ (V) and $U_0 = 34.1\,\mathrm{m/s}$ (VII) are almost similar.

The measured data for boundary layers I–IV and VIII were fitted with a laminar Blasius profile [27]. A good fit is obtained for profile I at 4 m/s. For increasing velocities, boundary layers II–IV and VIII, the deviation from a Blasius profile appeared to become significant. The profiles V–VII and IX and X are fitted with a turbulent boundary layer velocity distribution given by the logarithmic law corrected with Coles' law of the wake [28]:

$$\frac{U(y)}{u_{\mathrm{fric}}} = \frac{1}{\kappa}\ln\left(\frac{u_{\mathrm{fric}} y}{\nu}\right) + B + \frac{\Pi}{\kappa}\left(1 - \cos\left(\pi\frac{y}{\delta_{\mathrm{tu}}}\right)\right), \quad y \leqslant \delta_{\mathrm{tu}},$$
$$\Pi = \frac{\kappa}{2}\frac{U_0}{u_{\mathrm{fric}}} - \frac{1}{2}\ln\left(\frac{u_{\mathrm{fric}}\delta_{\mathrm{tu}}}{\nu}\right) - \frac{B\kappa}{2}. \tag{16}$$

Here u_{fric} is the friction velocity. Table I gives the friction velocity obtained from the fit for the concerning boundary layers. $B = 5.1$ is a boundary layer constant, $\kappa = 0.41$ is the von Kármán constant, and δ_{tu} is the turbulent boundary layer thickness where $U(\delta_{\mathrm{tu}}) = U_0$. Good agreement between the measured profiles and the fits was obtained.

In order to investigate the turbulence of the boundary layers some more, the turbulent intensity Tu is considered. Following, e.g. Schlichting [27]), we define the turbulence intensity here as the ratio of the root mean square of the turbulent velocity fluctuations $U' = \sqrt{U_x'^2 + U_y'^2}$ perpendicular to the hot-wire and the velocity U_0 outside the boundary layer:

$$\mathrm{Tu} = \frac{\sqrt{\langle U'^2\rangle}}{U_0}. \tag{17}$$

The turbulence intensity of the turbulent fitted boundary layers (i.e. numbers V, VI, VII, IX and X) is indeed found to be larger than that of the laminar fitted boundary layers. However, especially for boundary layers IV and VIII the turbulence intensity is found to be almost as large as for the turbulent fitted ones: $\mathrm{Tu} \simeq 0.1$ at maximum. Although it is still reasonably well fitted with a laminar Blasius profile, these boundary layers can be regarded as on the transition from laminar to turbulent. Also, when looking at the time signals of the hotwire measurements, the velocity fluctuations were found to occur more rapidly with increasing main flow velocity for the laminar fitted boundary layers. And indeed the velocity fluctuations for the turbulent fitted boundary layers were found to occur much more rapidly than for all laminar fitted boundary layers.

Summarizing the results above, boundary layers I–III will be regarded as laminar, whereas boundary layers IV and VIII are designated transitional. The sandpaper tripped boundary layers V, VII and IX are turbulent. Due to the observed pronounced form of a wake behind a object the spoiler tripped boundary layers VI and X will be designated as turbulent wake.

5.2. Shear layer profiles

In studying its acoustical response the flow properties of the shear layer developing in the orifice are of interest. Therefore, hot-wire measurements of shear layer profiles are done for the 1 cm orifices with double

sharp 27° edges and with double 90° edges, as well as the 5 cm slit, cf. Fig. 5a, d and e, respectively. Results for the 1 cm slot with sharp edges are shown in Fig. 6 for boundary layer flows I–V. Shear layer profiles at various distances from the upstream edge x_s are depicted, viz. $x_s = 2$ mm, $x_s = 4$ mm, $x_s = 6$ mm and $x_s = 8$ mm. Also the boundary layer profiles are shown ($x_s = 0$ mm). The y-coordinate on the horizontal axes is scaled to the momentum thickness θ_0 of the boundary layer. Shear layer profiles for the 1 cm slot with double 90° edges are shown in Fig. 7 at the same distances x_s for transitional boundary layer flow IV and turbulent boundary layers

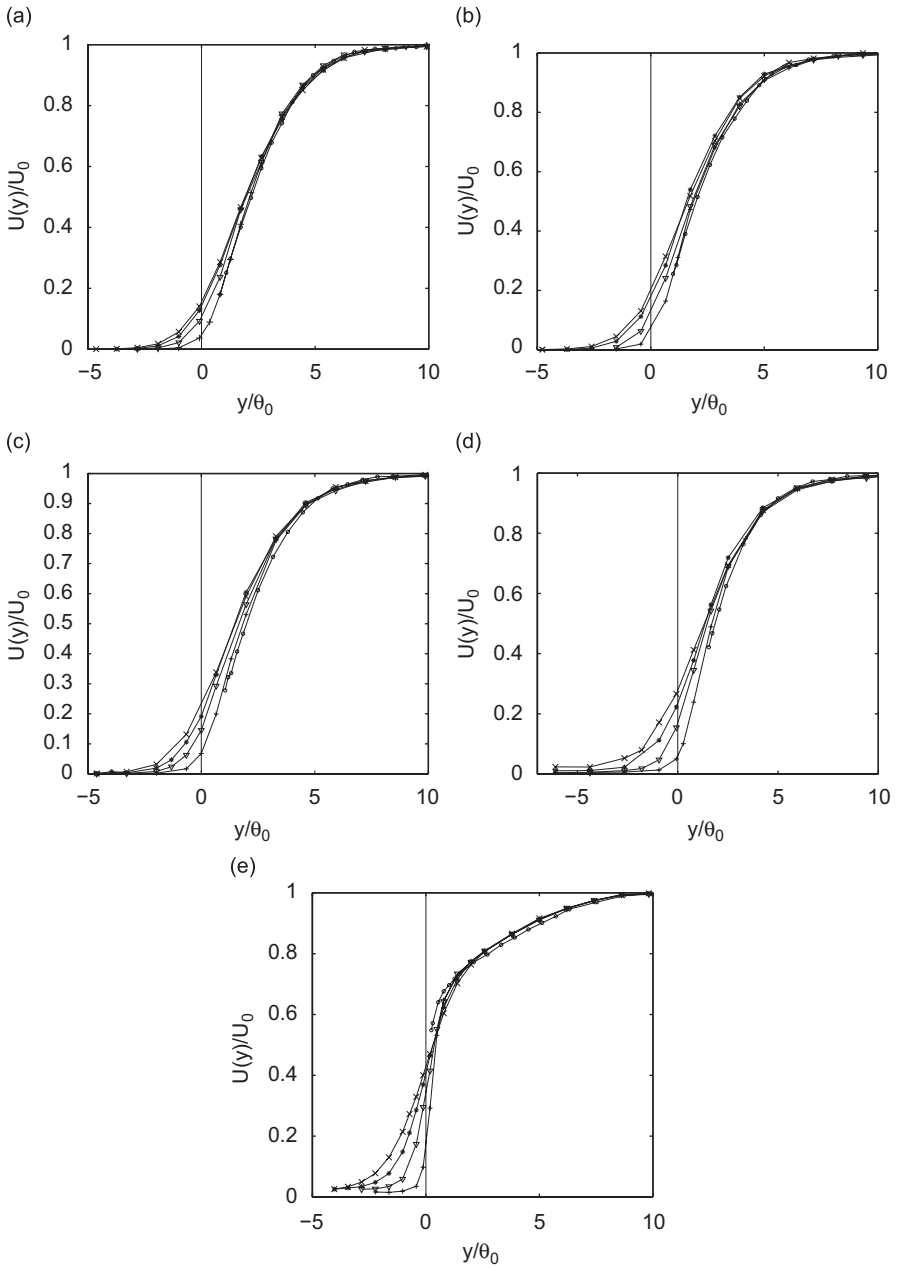

Fig. 6. Shear layer profile measurements at various distances x_s from the upstream edge for the 1 cm slot with double 27° edges, cf. Fig. 5a, and different boundary layer flows, see Table 1: (a) BL I; (b) BL II; (c) BL III; (d) BL IV; (e) BL V. Symbols: ○, $x_s = 0$ mm (boundary layer profile); +, $x_s = 2$ mm; ∇, $x_s = 4$ mm; ∗, $x_s = 6$ mm; ×, $x_s = 8$ mm. The y-coordinate is scaled to the boundary layer momentum thickness θ_0.

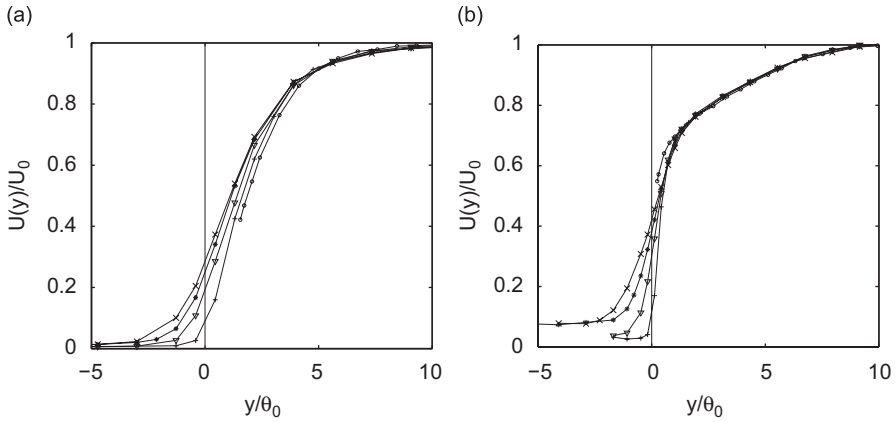

Fig. 7. Shear layer profile measurements at various distances x_s from the upstream edge for the 1 cm slot with double 90° edges, cf. Fig. 5d, and different boundary layer flows, see Table 1: (a) BL IV; (b) BL V. Symbols: ○, $x_s = 0$ mm (boundary layer profile); +, $x_s = 2$ mm; ∇, $x_s = 4$ mm; ∗, $x_s = 6$ mm; ×, $x_s = 8$ mm. The y-coordinate is scaled to the boundary layer momentum thickness θ_0.

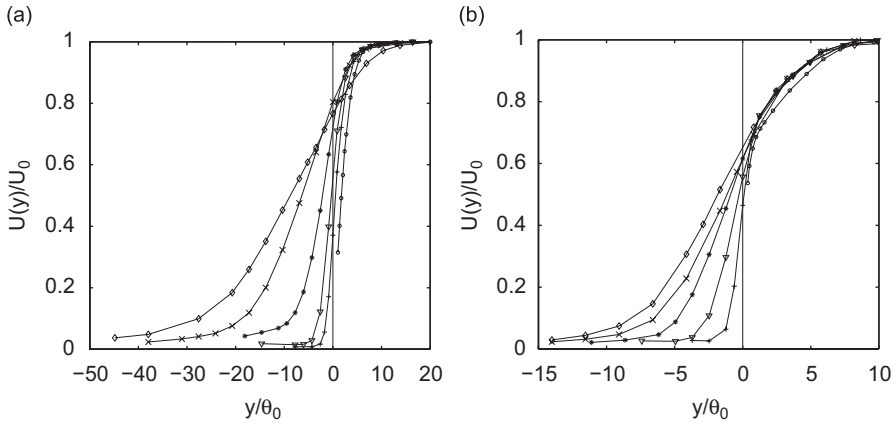

Fig. 8. Shear layer profile measurements at various distances x_s from the upstream edge for the 5 cm slot with double 90° edges, cf. Fig. 5e, and different boundary layer flows, see Table 1: (a) BL VIII; (b) BL IX. Symbols: ○, $x_s = 0$ mm (boundary layer profile); +, $x_s = 5$ mm; ∇, $x_s = 10$ mm; ∗, $x_s = 20$ mm; ×, $x_s = 30$ mm; ◇, $x_s = 40$ mm for BL VIII or $x_s = 35$ mm for BL IX. The y-coordinate is scaled to the boundary layer momentum thickness θ_0.

V. For the 5 cm slot shear layer profiles for boundary layer flows VIII and IX (to be compared with boundary layers IV and V for the 1 cm slots) are shown in Fig. 8 for various distances x_s from the upstream edge. The shear layer profiles (of boundary layers IV and V) for the 1 cm slot with sharp edges and the 1 cm slot with normal edges are nearly identical. However, for turbulent boundary layer flow V the measured velocity does not seem to tend to zero at the lower side of the shear layer in case of the slot with normal edges. Here, the flow velocity remains more or less constant. Most probably this is caused by the fact there is a significant entrainment velocity. Comparing the geometries of the two orifices it could be expected that the flow in the slot with normal edges will differ more from an 'ideal' parallel shear flow especially near the upstream and downstream edge. In the case of normal edges the entrainment velocity will have a strong component perpendicular to the main flow. The effect is also seen in shear layer measurements closest to the upstream edge for the 5 cm slot especially with turbulent boundary layer IX. Analogous to the boundary layer momentum thickness, the shear layer momentum thickness is given by:

$$\theta = \int_{-\infty}^{\infty} \frac{U(y)}{U_0}\left(1 - \frac{U(y)}{U_0}\right) \mathrm{d}y. \tag{18}$$

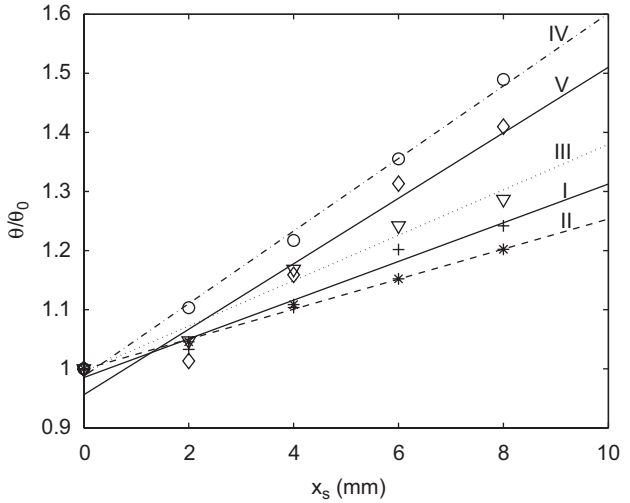

Fig. 9. Shear layer momentum thickness θ scaled by the corresponding boundary layer momentum thickness θ_0 against distance x_s from the upstream edge for the 1 cm slot with double 27° edges. Symbols: +, BL I; ∗, BL II; ∇, BL III; ○, BL IV; ◇, BL V. A linear fit is applied to each data series.

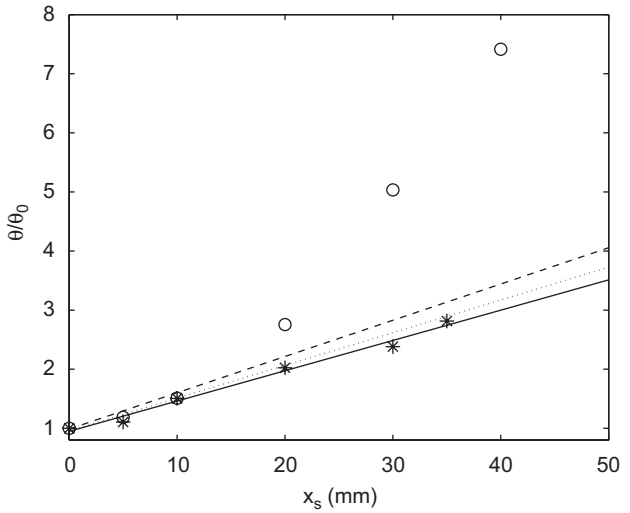

Fig. 10. Shear layer momentum thickness θ scaled by the corresponding boundary layer momentum thickness θ_0 against distance x_s from the upstream edge for the 5 cm slot. Symbols: ○, BL VIII; ∗, BL IX. Solid line: linear fit of data for BL IX. Dashed and dotted line: linear fit of data for BL IV and BL, respectively, V in case of 1 cm slot with sharp edges, cf. Fig. 9.

The momentum thickness as function of the distance from the upstream edge calculated for the experimental data above is shown in Fig. 9 for the 1 cm slot with sharp edges for boundary layer flows I–V. For all boundary layer flows the data can be fitted well with a straight line, giving a linear increase of momentum thickness with distance. For the 5 cm slot momentum thickness as function of distance to upstream edge is depicted in Fig. 10. For the turbulent boundary layer IX a linear fit applies. As shown in the graph this fit agrees well with that applied to the data for the corresponding turbulent boundary layer V in case of the 1 cm slot with sharp edges (Fig. 9). For the transitional boundary layer VIII a linear increase in momentum thickness with distance is seen up to $x_s = 10$ mm. The linear fit applied to the data of the corresponding transitional boundary layer IV in case of the 1 cm slot with sharp edges, cf. Fig. 9, also applies reasonably well to these points. However, for larger distances from the upstream edge a stronger increase in momentum

thickness is seen. Note that, in calculating the momentum thickness, for those cases in which a non-zero velocity is measured at the lower side of the shear layer due to the entrained normal velocity, an estimate of the (parallel) profile there is made. The error in the calculated values for θ/θ_0 is estimated at $\pm 5\%$. Due to experimental constraints the shear layer profiles for the spoiler tripped turbulent wakes VI and X have not been measured.

6. Results

6.1. Impedance without mean flow

The experimental set-up used, cf. Fig. 3, i.e. an orifice in a plate placed close to a windtunnel outlet in a room which is only anechoic above 300 Hz, is acoustically rather complex. In order to determine the effect of grazing mean flow on the orifice impedance, according to Eq. (7), later on, the impedance in absence of flow has been measured. Results are shown in Fig. 11. Here, as reference, the real part of the impedance, i.e. the resistance r, is scaled to the square of the Helmholtz number k_0R_e based on the hydraulic radius R_e of the aperture. The imaginary part of the impedance is scaled to the Helmholtz number k_0R_e. The hydraulic radius of the orifice is the equivalent radius of a circular orifice with the same area: $R_e = \sqrt{S_0/\pi}$. At low frequency the resistance becomes very small, resulting in a relatively large measurement error. Furthermore, the scaling factor $(k_0R_e)^2$ tends to 0 for low frequency. This results in the large value for the scaled resistance at low frequency shown in Fig. 11. Note that in presence of grazing flow the resistance at low frequency becomes much larger than in case of no flow (see e.g. Fig. 13 further on), so that the relative measurement error greatly reduces.

Between a frequency of $f = 200$ and 800 Hz, corresponding to k_0R_e between 0.05 and 0.2, the value for the scaled resistance is reasonably constant between 0.5 and 1. Also, results for the different orifice geometries are in general quite close. For higher frequency large values or the resistance are seen. According to Eq. (4), the imaginary part of the impedance divided by Helmholtz number k_0R_e equals the ratio of reactance δ to hydraulic radius R_e. Except at higher frequencies the observed values in Fig. 11 are fairly constant with frequency for all orifice geometries.

The reactance is a measure of the total amount of fluid effectively participating in the acoustic motion in the orifice. In this respect the value of the reactance for the different orifice geometries increases as expected in the following order: double sharp 27° edges, single sharp 27° edge, single sharp 0° edge and normal 90° edges. For the orifice with normal 90° edges the plate thickness (equal to 1.5 cm, or $1.19R_e$) can simply be subtracted from the reactance δ to obtain an end correction. This end correction is then about equal to the hydraulic radius R_e.

An indication of the accuracy of reflection coefficient measurements, addressed in Section 3.3 above, in relation to the orifice impedance without flow is given in Fig. 12. Here, the reflection coefficient R in case the orifice impedance is $Z_{h-} = 0.5(k_0R_2)^2 + \mathrm{i}1.8k_0R_e$ is compared to the error in the reflection coefficient at a closed wall. Note that this impedance is representative for an orifice in free space (in absence of mean flow).

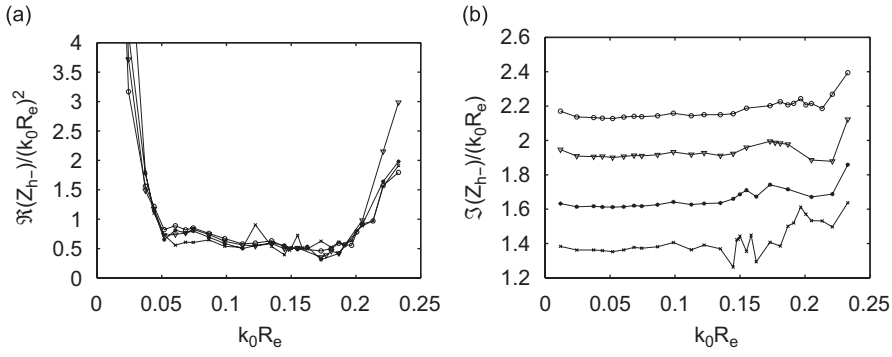

Fig. 11. Real part (a) and imaginary part (b) of the aperture impedance Z_{h-}, scaled to the Helmholtz number squared resp. the Helmholtz number, for the slots with different edge geometries, cf. Fig. 5. Symbols: ×, double sharp 27° edges; ∗, single sharp 27° edge; ○, normal 90° edges; ∇, single sharp 0° edge.

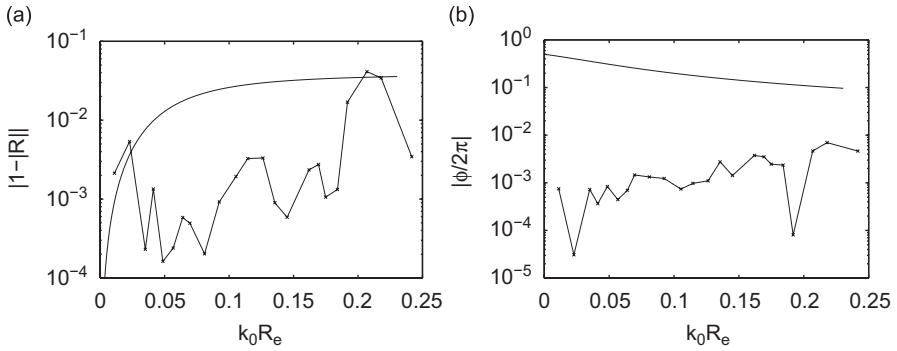

Fig. 12. Magnitude (a) and phase (b) of the reflection coefficient R for an impedance $Z_{h-} = 0.5(k_0R_e)^2 + \mathrm{i}1.8k_0R_e$, representative for the results displayed in Fig. 11, (solid line) compared to the error in R in case of a closed end wall (× symbols), cf. Fig. 4.

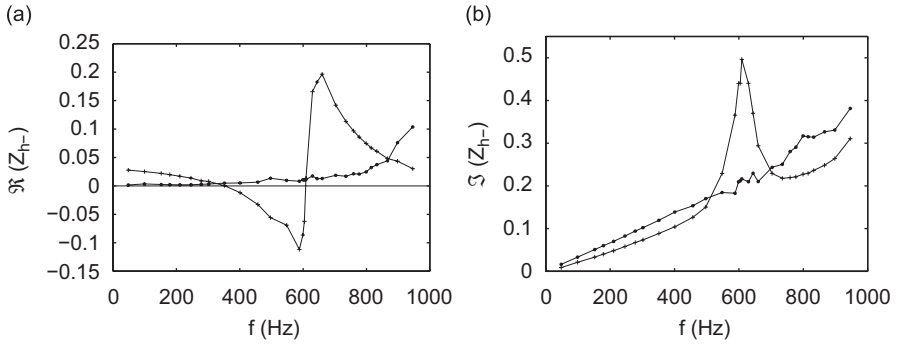

Fig. 13. Real part (a) and imaginary part (b) of the aperture impedance Z_{h-} for the $L = 1$ cm slit with double sharp 27° edges without flow (∗ symbols) and with grazing flow (+ symbols) as function of frequency f in case of turbulent boundary layer V.

However, it is not necessarily representative for the current set-up, as it is acoustically more complex (see the remark above). For instance resonances in the windtunnel exit nozzle (measuring 20 cm × 20 cm) are to be expected around $f = 860$ Hz. Such resonances can greatly modify the orifice impedance. The figure shows the value of $|1 - |R||$ and $|\phi/2\pi|$, with ϕ the phase of the reflection coefficient, for both the orifice impedance mentioned above and for the measurements at a closed wall, cf. Fig. 4, as function of Helmholtz number k_0R_e. It is observed that for low and high frequency the deviation of the absolute value of the reflection coefficient from unity, calculated for the mentioned impedance, is of the same order as the error. In between the error is about an order in magnitude smaller than the value related to the given impedance. The error in the phase of the reflection coefficient is at least an order of magnitude smaller than the value related to the given impedance.

6.2. Impedance with grazing mean flow

Fig. 13 shows the measured impedance Z_{h-}, cf. Eq. (3), for the $L = 1$ cm orifice with double sharp 27° edges as function of frequency f in case no mean flow is present, and in case of grazing mean flow with turbulent boundary layer V. Globally, for this particular boundary layer case the effect of the grazing flow on the impedance is quite large compared to the value of the impedance without flow. The difference in impedance due to the flow is depicted in Fig. 14. With grazing flow the value of the impedance (both real and imaginary part) oscillates around the no flow value. At low frequency the flow increases the resistance, here absorption of sound occurs. For increasing frequency this effect diminishes, and at around $f = 320$ Hz a region starts where the resistance is decreased by the grazing flow. In this region the resistance with flow becomes negative, this means sound production takes place. At about $f = 590$ Hz there is a minimum in the resistance, after which a

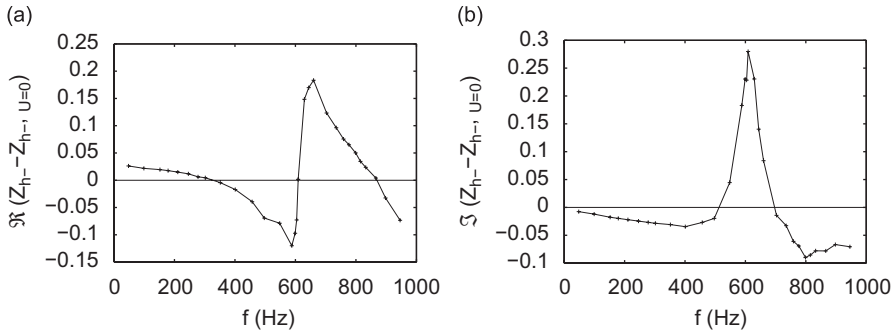

Fig. 14. Change of the real part (a) and imaginary part (b) of the aperture impedance Z_{h-} due to grazing flow as function of frequency f for the 1 cm orifice with double sharp 27° edges with turbulent boundary layer V.

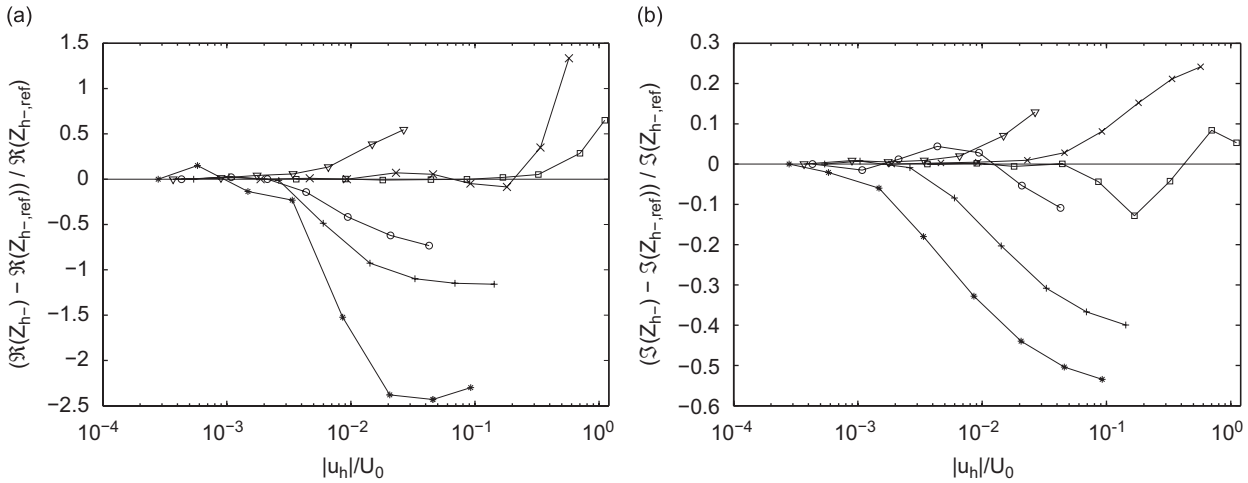

Fig. 15. Relative change of the real (a) and imaginary part (b) orifice impedance Z_{h-} with respect to a reference value $Z_{h-,\mathrm{ref}}$ for the 1 cm orifice with double sharp 27° edges in case of turbulent boundary layer V as function of the amplitude of the acoustic velocity through the orifice $|u_h|$ over the mean flow velocity U_0. For $Z_{h-,\mathrm{ref}}$ the value at the lowest acoustic velocity amplitude is taken. Symbols: □, $f = 48$ Hz; ×, $f = 302$ Hz; +, $f = 588$ Hz; ∗, $f = 609$ Hz; ○, $f = 660$ Hz; ∇, $f = 898$ Hz.

sharp transition to a second region of sound absorption is seen. The increase in resistance due to the flow in this region is much larger than at low frequencies. The sharp transition in the resistance coincides with a peak in the imaginary part of the impedance. In a region around this peak the effect of the flow is to increase the imaginary part of the impedance, and therefore the reactance, whereas outside this region the reactance is decreased by the flow.

6.3. Linearity

The linearity of orifice impedance with grazing flow is investigated by measuring at different sound pressure levels. Results for the $L = 1$ cm slot with double sharp 27° edges with turbulent boundary layer V at several frequencies are plotted in Fig. 15. The graphs show the relative change of the real and imaginary part of the orifice impedance Z_{h-} with respect to a reference value $Z_{h-,\mathrm{ref}}$ as function of the amplitude of the acoustic velocity through the orifice $|u_h|$ over the mean flow velocity U_0. The value of the impedance at the lowest acoustic velocity amplitude is taken as reference $Z_{h-,\mathrm{ref}}$. Note that the scale $|u_h|/U_0 = 10^{-4}$ to $|u_h|/U_0 = 1$ in Fig. 15 corresponds to sound pressure levels from about 70 dB up to 150 dB just beneath the orifice.

For the lowest frequency, $f = 48$ Hz, linear behaviour is observed up to a relative amplitude $|u_h|/U_0 = 0.2$ for the real part and up to $|u_h|/U_0 = 5 \times 10^{-2}$ for the imaginary part of the impedance. At $f = 302$ Hz, just

before the resistance becomes negative, see Fig. 13, impedance is linear up to a relative amplitude $|u_h|/U_0$ of 10^{-2}. Strong nonlinear behaviour is only seen for $|u_h|/U_0$ larger than 0.1. For the frequencies $f = 588$ and 660 Hz, at which the resistance has a minimum and maximum, respectively, cf. Fig. 13, the onset of nonlinear behaviour is at approximately $|u_h|/U_0 = 2 \times 10^{-3}$. For $f = 609$ Hz, corresponding to the sharp transition from negative to positive resistance and the peak in the imaginary part of the impedance, cf. Fig. 13, the onset of nonlinearity seems to be at even lower amplitude, at about $|u_h|/U_0 = 3 \times 10^{-4}$. At a frequency of $f = 898$ Hz, beyond the strong oscillations in impedance, linearity is observed up to $|u_h|/U_0$ several times 10^{-3}.

Considering the deviations in the impedance from the (linear) reference value at a given amplitude, the effect of nonlinearity increases from $f = 48$ Hz to subsequently $f = 302, 898, 660, 588, 609$ Hz. Nonlinearity thus seems to be strongest in the region where the oscillations in impedance are observed, here the onset of nonlinear behaviour is at lower amplitudes and the deviation from the linear impedance is largest.

In following measurements on the linear behaviour of the orifice impedance under grazing flow the acoustic amplitudes mostly are close to the onset of nonlinearity, in order to have maximum signal amplitude.

6.4. Non-dimensional scaled resistance and reactance

Figs. 16 and 17 show the non-dimensional scaled resistance and reactance, as defined in Eq. (7), for the $L = 1$ cm orifice with double 27° edges for the different boundary layer flows. Non-dimensional scaled resistance and reactance for the $L = 5$ cm aperture are depicted in Fig. 18. The results are plotted versus the Strouhal number $\omega L/U_0$ based on the orifice width in stream wise direction and the main flow velocity outside the boundary layer. For the $L = 1$ cm orifice similar features are seen for all boundary layers. For increasing Strouhal number about 4 regions are observed. For low Strouhal number resistance is positive, implying sound absorption. For higher Strouhal number a region is found where resistance is negative, implying sound production due to the grazing flow. Subsequently two more regions of alternately positive and negative resistance follow. A similar oscillating behaviour is seen for the reactance. For both resistance and reactance the oscillations damp out for high Strouhal number. The Strouhal numbers of the oscillations in the reactance more or less coincide with those of the oscillations in the resistance. These specific features in resistance and reactance generally shift to a higher Strouhal number for decreasing boundary layer thickness. Furthermore, the amplitudes of the oscillations increase with decreasing laminar/transitional boundary layer thickness (I–IV). For the turbulent boundary layer V larger oscillations in the resistance and reactance are observed than for the laminar boundary layers I–III, although the boundary layer thickness of V is generally larger than that of I–III. For the spoiler tripped turbulent wake VI qualitatively the same features for the resistance and reactance as discussed are observed up to a Strouhal number of 1.7. However, for larger Strouhal number especially the resistance is not found to damp out to 0 (at least up to the largest Strouhal number measured). The results for turbulent boundary layer flows V and VII, which have nearly the same characteristics but different Mach number, are very close, although the first 'peak' of negative resistance at $\omega L/U_0 \simeq 2$ is stronger for BL VII.

For the $L = 5$ cm orifice more oscillations in resistance and reactance are found. Furthermore, for the turbulent wake boundary layer X less clearly defined behaviour is found. In this case the error in the measurements is of the same order as the measured effect itself. For the transitional boundary layer VIII, the thinnest one, most oscillations are seen. Also the oscillations are at a higher Strouhal number and have a larger amplitude compared to the turbulent boundary layer IX case. This is the same as seen in mutually comparing the correspondent boundary layers IV and V, respectively, for the $L = 1$ cm orifice. Furthermore, in the results for transitional and turbulent boundary layers VIII and IX, respectively, the first resonance in resistance and reactance has a smaller amplitude and seem to be at a slightly higher Strouhal number, compared to their corresponding cases for the $L = 1$ cm slot.

6.5. Effective Strouhal number

As pointed out by others, e.g. Golliard [14], the impedance of the orifice is closely connected to the hydrodynamic instability of the shear layer developing in the orifice. A better way to compare

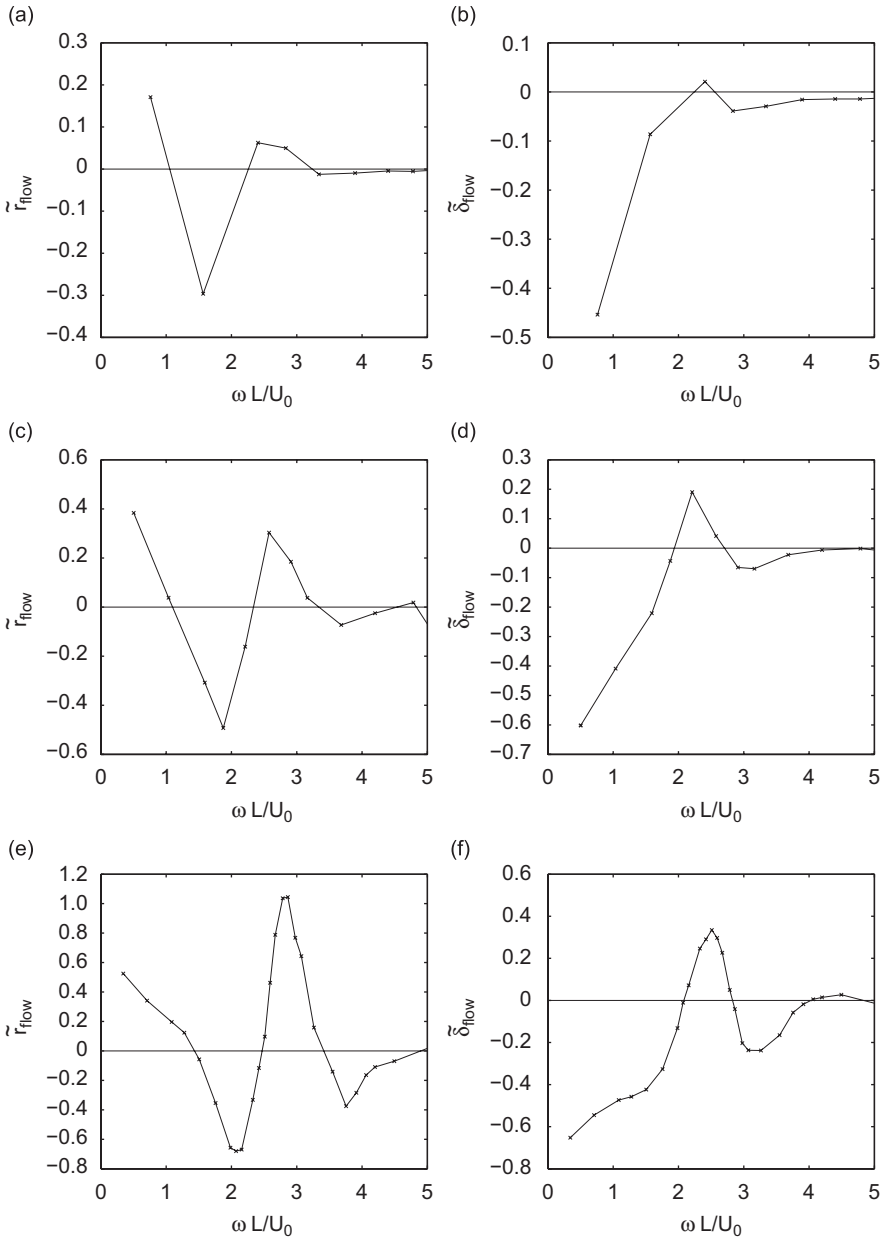

Fig. 16. Non-dimensional scaled resistance $\tilde{r}_{flow}$ resp. reactance $\tilde{\delta}_{flow}$ due to grazing mean flow for the $L = 1$ cm orifice with double 27° edges for different boundary layer flows (the boundary layer momentum thickness θ_0 scaled to the slit width L is indicated for each case): (a,b) BL I, $\theta_0/L = 0.055$; (c,d) BL II, $\theta_0/L = 0.046$; (e,f) BL III, $\theta_0/L = 0.038$.

orifice impedance for different boundary layers would therefore be to consider them as a function of the Strouhal number based on the phase velocity U_c of the hydrodynamic instability wave, i.e. the convection velocity of vorticity in the aperture, rather than as function of the Strouhal number based on the main flow velocity U_0. Golliard [14] used the convection velocity as a fit parameter to get a better agreement with the theoretical prediction of Howe [15]. Goldman and Panton [2] for instance also discussed the use of an effective convection velocity, although they gave it a more general interpretation.

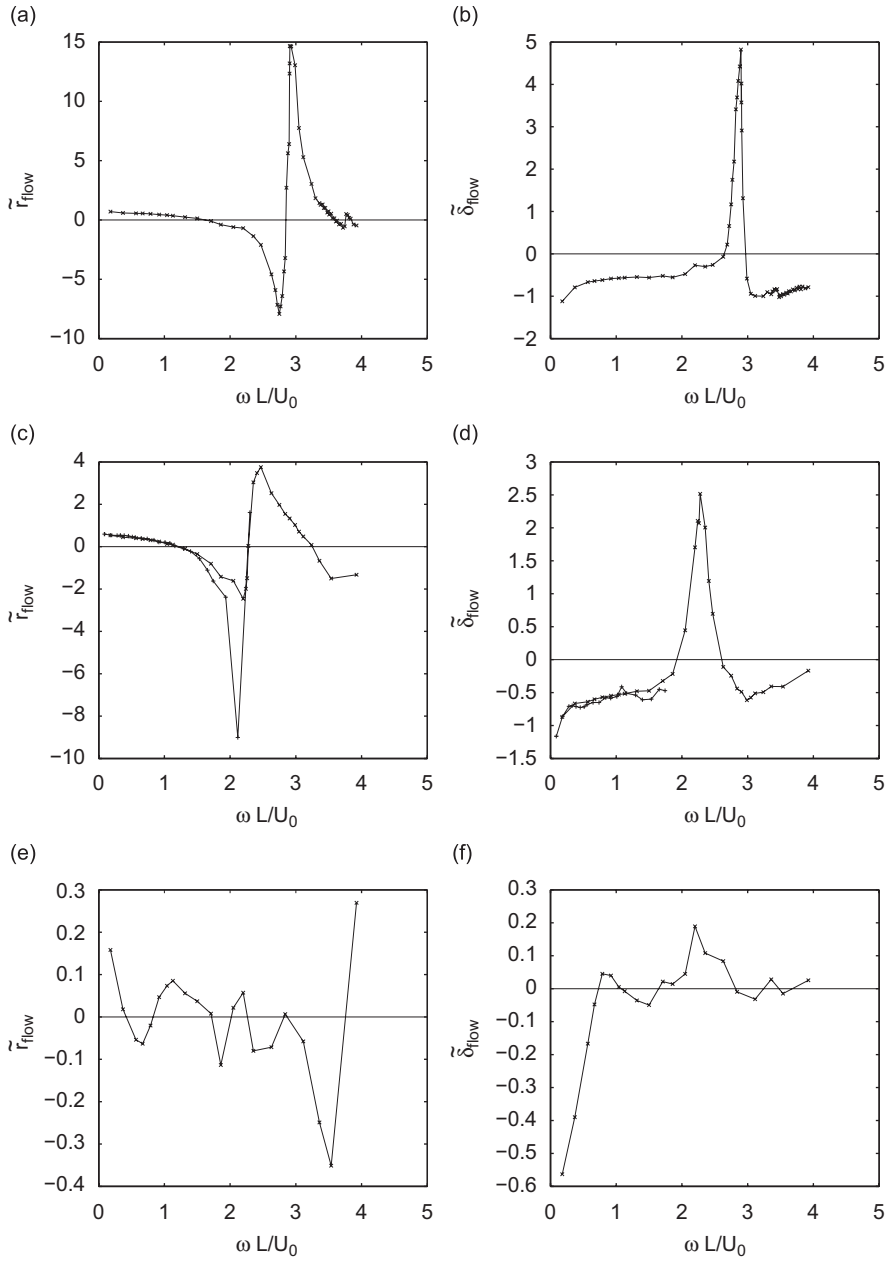

Fig. 17. Non-dimensional scaled resistance $\tilde{r}_{flow}$ resp. reactance $\tilde{\delta}_{flow}$ due to grazing mean flow for the $L = 1$ cm orifice with double 27° edges for different boundary layer flows (the boundary layer momentum thickness θ_0 scaled to the slit width L is indicated for each case): (a,b) BL IV, $\theta_0/L = 0.029$; (c,d) ×: BL V, $\theta_0/L = 0.083$; +: BL VII, $\theta_0/L = 0.081$; (e,f) BL VI, $\theta_0/L = 0.39$.

Here we attempt to use calculations of the convective velocity of hydrodynamic instability in a shear layer with generalized hyperbolic-tangent form as presented by Michalke [29,30]:

$$\frac{U(y)}{U_0} = 1 - (1 + m\mathrm{e}^{mf(m)y/\theta})^{-1/m},$$
$$f(m) = \int_0^1 \frac{1-z}{1-z^m}\,\mathrm{d}z. \tag{19}$$

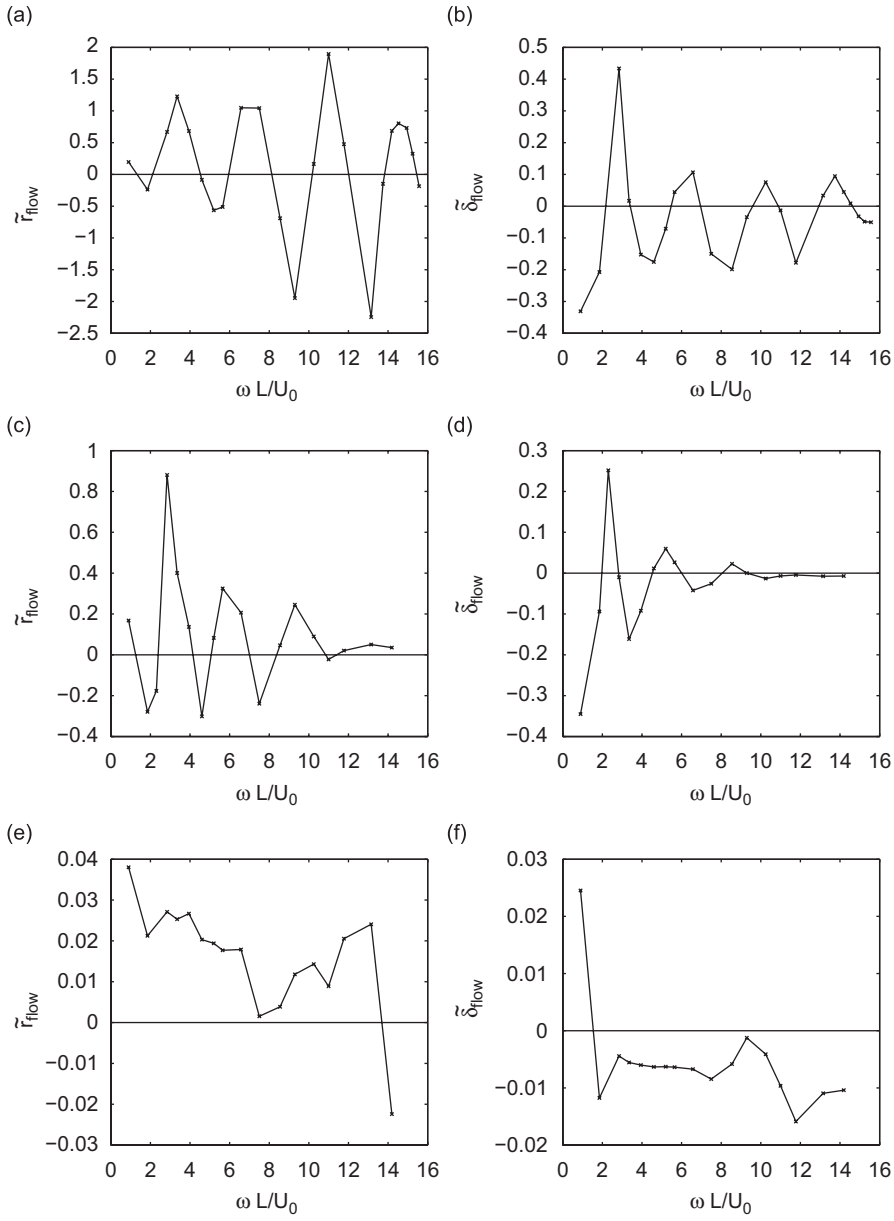

Fig. 18. Non-dimensional scaled resistance $\tilde{r}_{\text{flow}}$ resp. reactance $\tilde{\delta}_{\text{flow}}$ due to grazing mean flow for the $L = 5$ cm orifice for different boundary layer flows (the boundary layer momentum thickness θ_0 scaled to the slit width L is indicated for each case): (a,b) BL VIII, $\theta_0/L = 0.0055$; (c,d) BL IX, $\theta_0/L = 0.0162$; (e,f) BL X, $\theta_0/L = 0.0725$.

As shown there, for given profile, set by the profile parameter m, the phase velocity U_c of the hydrodynamic instability, non-dimensionalized by the mean flow velocity U_0, is a function of the Strouhal number based on the momentum thickness θ of the shear layer and U_0:

$$\frac{U_c}{U_0} = f\left(\frac{\omega\theta}{U_0}, m\right). \tag{20}$$

Generally, concerning the form of the shear layers, it was found that generally a good fit could be obtained between experiments, cf. Figs. 6–8, and the generalized hyperbolic-tangent profile, Eq. (19).

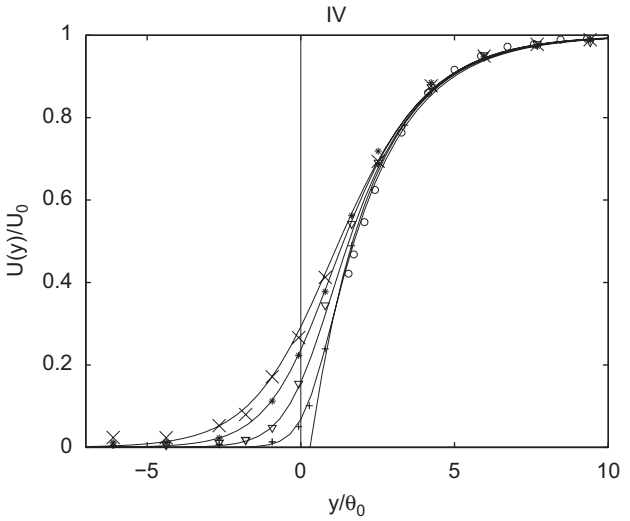

Fig. 19. Measured shear layer profiles for the 1 cm wide orifice with double 27° edges with transitional boundary layer flow IV, cf. Fig. 6, fitted with the tangent hyperbolic profile (solid lines), Eq. (19), for different distances from upstream edge x_s. Symbols: ○, $x_s = 0$ mm (boundary layer profile), $\theta = \theta_0 = 0.29$ mm, profile parameter $m = \infty$; +, $x_s = 2$ mm, $\theta = 0.32$ mm, $m = 5$; ∇, $x_s = 4$ mm, $\theta = 0.35$ mm, $m = 3$; ∗, $x_s = 6$ mm, $\theta = 0.39$ mm, $m = 2$; ×, $x_s = 8$ mm, $\theta = 0.44$ mm, $m = 1.5$.

This is illustrated in Fig. 19, where the measured shear layer profiles for the 1 cm orifice with double 27° edges and transitional boundary layer flow IV are fitted with Eq. (19). The values of the shear layer momentum thickness used in the fits is close to those calculated from the measured profiles, cf. Fig. 9. As shown, the profile parameter m varies between ∞ for the boundary layer to $m = 1.5$ for the shear layer 8 mm from the upstream edge. The hyperbolic-tangent profiles are shifted in the y-direction as to give the best fit with experimental data. For the boundary layer this actually gives a slight offset in the wall position. Note that shifting the fit profiles does not affect the calculated phase velocity.

For the turbulent boundary layer flows, no. V for the 1 cm slots and no. IX for the 5 cm slot and for the 5 cm slot with transitional boundary layer flow VIII shear layer profiles could be fitted less well with the generalized hyperbolic-tangent profile than shown in the figure above.

Despite the good fit of the measured shear layer profiles with the generalized hyperbolic-tangent profile, the form of the shear layer changes and the momentum thickness increases with distance from the upstream edge, such that no unambiguous convection velocity can be found here. Nevertheless, as first approximation for the averaged convection velocity of vorticity in the orifice can be derived from the shear layer profile halfway the orifice. A reasonable justification for this can be found in the fact that the momentum thickness of the shear layer increases linearly with distance x_s from the upstream orifice edge (except for BL VIII, cf. Fig. 10), and that the convection velocity on its turn depends almost linearly on the Strouhal number based on the momentum thickness, $\omega\theta/U_0$ (certainly for $\omega\theta/U_0 \lesssim 0.15$) [30]. Furthermore, for low profile parameter, $m \lesssim 4$, which is generally applicable to the measured profiles, the difference found in convection velocity between profiles with different m is 20% at maximum.

A scaling of the Strouhal number based on the above mentioned is done for the experiments with the 1 cm slit with double 27° edges for boundary layer flows I–V, depicted in Figs. 16 and 17. The convective velocity is thus calculated from Michalke's results for a shear layer profile halfway the slot, at $x_s = 5$ mm. The profile parameter is taken $m = 2$, providing a reasonably good fit with measured shear layer profiles. The momentum thickness at $x_s = 5$ mm is determined from Fig. 9.

Note that here only the range $\omega\theta/U_0 < 0.25$, for which U_c is given, is considered. For comparison the resistance and reactance for the 1 cm slot versus Strouhal number $\omega L/U_0$ for boundary layer flows I–V, cf. Figs. 16 and 17, are plotted together in Fig. 20. The same results plotted versus Strouhal number on the convective velocity are displayed together in Fig. 21. Here, the resistance and reactance are scaled to the average of their absolute value for each case. In the same way, scaling of the results for the $L = 5$ cm aperture

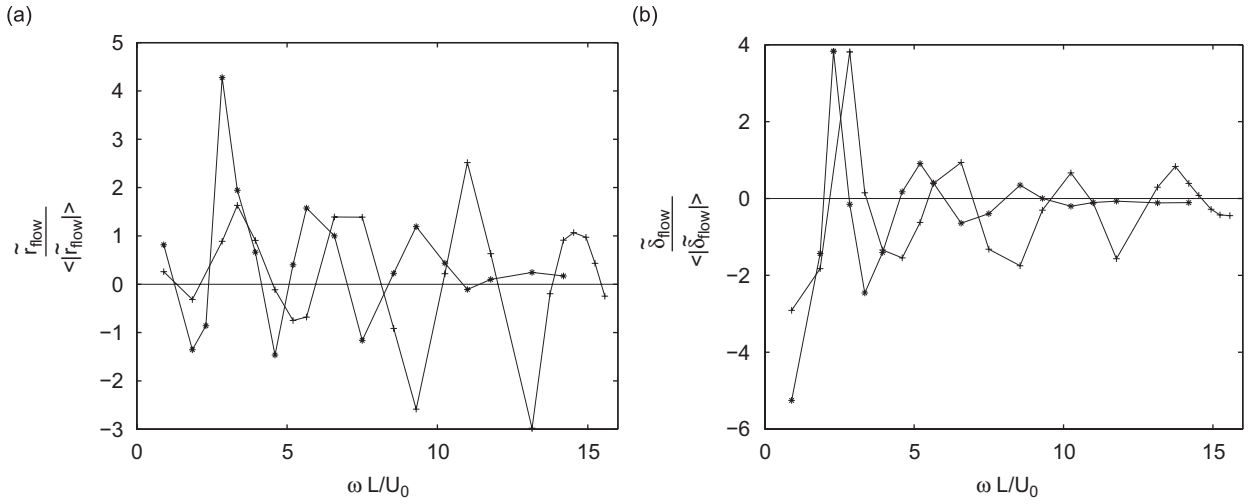

Fig. 20. Non-dimensional scaled resistance (a) and reactance (b) for the $L = 1$ cm orifice with double 27° edges for boundary layers I–V against Strouhal number on the mean flow velocity U_0: data of Figs. 16 and 17. The resistance and reactance are scaled to the average of their absolute value. Symbols: ◇, BL I; ∗, BL II; ∇, BL III; ○ BL IV; ×, BL V.

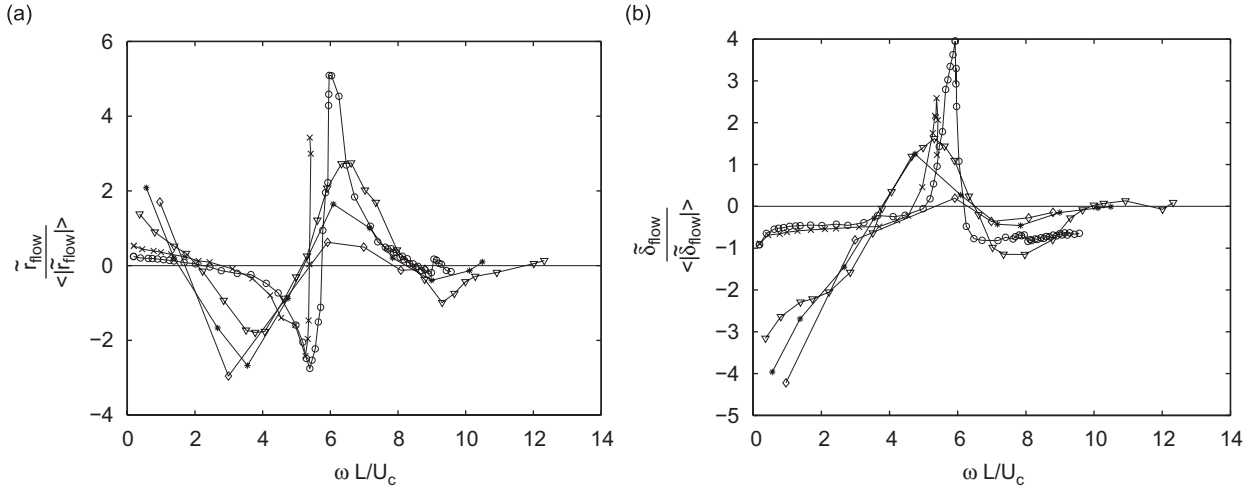

Fig. 21. Non-dimensional scaled resistance (a) and reactance (b) for the $L = 1$ cm orifice with double 27° edges for boundary layers I–V against Strouhal number based on the convective velocity U_c. The resistance and reactance are scaled to the average of their absolute value. Symbols: ◇, BL I; ∗, BL II; ∇, BL III; ○, bL IV; ×, BL V.

with transitional boundary layer flow VIII and sandpaper tripped turbulent boundary layer flow IX, depicted in Fig. 18, is performed. Also here the hyperbolic-tangent profile parameter is taken $m = 2$, the momentum thickness is that halfway the slit, at $x_s = 25$ mm, cf. Fig. 10.

Again for comparison, the results for the 5 cm slot for boundary layer flows VIII and IX versus Strouhal number based on the mean flow velocity U_0, cf. Fig. 18, are plotted together in Fig. 22. The same results versus Strouhal number based on the convective velocity, are plotted together in Fig. 23. The resistance and reactance are scaled to the average of their absolute value for both cases. Looking at Fig. 20 and 21 for the $L = 1$ cm slot, the characteristic features in the non-dimensional scaled resistance and reactance are more at the same Strouhal number for the different boundary layers when using U_c instead of U_0. Especially the results for laminar boundary layers I–III 'coincide' very well. Also, the results for transitional boundary layer IV are much closer to those of the other boundary layers, when using the effective Strouhal number. Especially the

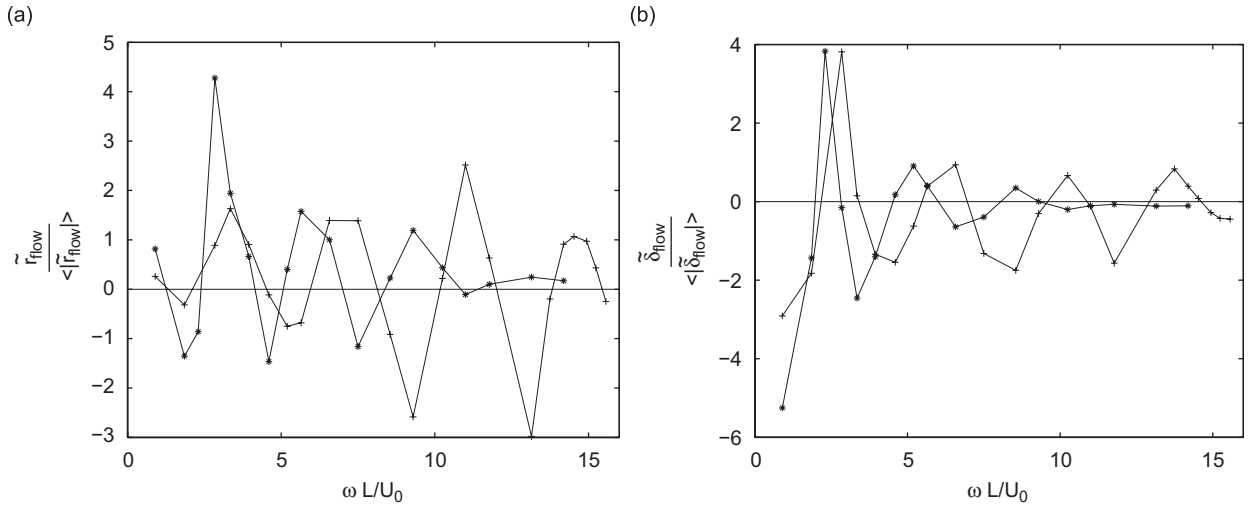

Fig. 22. Non-dimensional scaled resistance (a) and reactance (b) for the $L = 5$ orifice for transitional boundary layer VIII (+ symbols) and turbulent boundary layer IX (∗ symbols) versus Strouhal number based on the mean flow velocity U_0: data of Fig. 18. The resistance and reactance are scaled to the average of their absolute value.

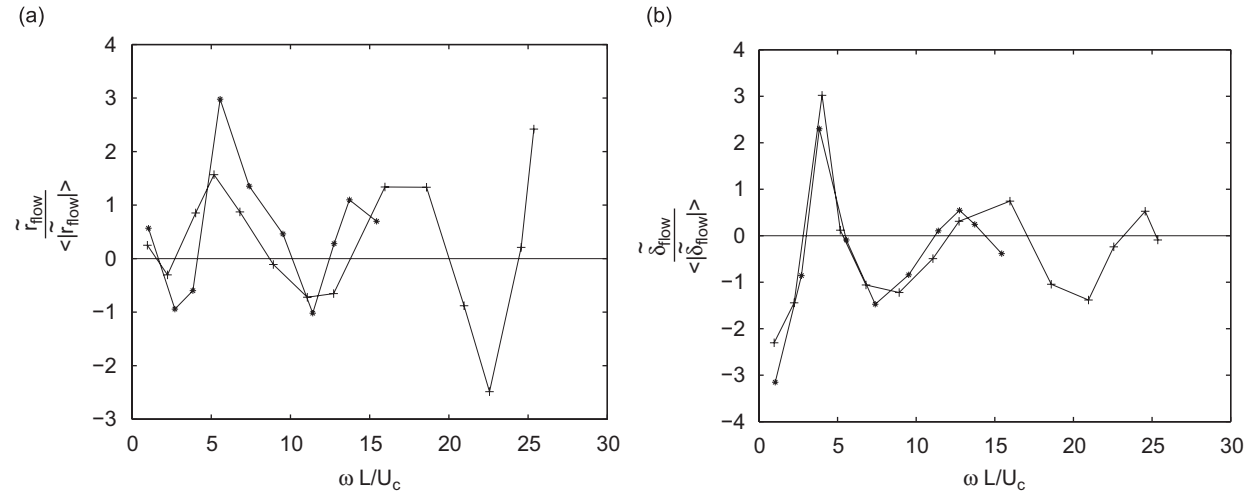

Fig. 23. Non-dimensional scaled resistance (a) and reactance (b) for the $L = 5$ orifice for transitional boundary layer VIII (+ symbols) and turbulent boundary layer IX (∗ symbols) versus Strouhal number based on the convective velocity U_c. The resistance and reactance are scaled to the average of their absolute value.

transition of negative to positive resistance and corresponding peak in reactance, around $\omega L/U_c = 5$, coincides better. In the region where resistance is negative results for transitional boundary layer IV and turbulent boundary layer V become very similar, when using the convective velocity. For the $L = 5$ cm slot, Figs. 22 and 23 show that using the convective velocity is mainly beneficial for the reactance, at least up to $\omega L/U_c = 13$. Comparing the results for the 1 cm slot and the 5 cm slot against Strouhal number on the convective velocity, the characteristic features seem to be at a slightly lower Strouhal number for the 5 cm slot. Furthermore, it was already observed that for the 5 cm slot still oscillations in resistance and reactance are seen for higher Strouhal numbers, where resistance and reactance tend to zero for the 1 cm slot. This could be explained by the fact that the ratio of boundary layer or shear layer momentum thickness θ to slot width L is much smaller for the 5 cm slot compared to the 1 cm slot. When assuming that oscillations in the non-dimensional scaled resistance and reactance (that is deviation from a zero value) can only occur when

hydrodynamic instability occurs, an estimate of the maximum Strouhal number where oscillations are still observed can be made. From Michalke [29,30] it follows that for a shear layer with generalized hyperbolic-tangent profile hydrodynamic instability occurs up to a Strouhal number on the momentum thickness, $Sr_\theta = \omega\theta/U_0$, of about 0.25. This value differs only slightly with profile parameter m. Using this, and the concerning ratios of boundary layer momentum thickness θ_0 (which is the minimum momentum thickness) to slit width L, the concerning maximum Strouhal number $\omega L/U_0$ is about 4.5, 5.4, 6.6, 8.6 and 3 for the 1 cm slot with boundary layer flows I–V, respectively. For the 5 cm slot the values are indeed much higher, namely 43 and 15 for the boundary layer flows VIII and IX, respectively. The above-mentioned numbers are fairly in agreement with what is observed in Figs. 20 and 22. It has to be noted that sandpaper tripped turbulent boundary layer flow V with the 1 cm slit seems to be a slight exception here, and for the 5 cm slot with transitional boundary layer VIII measurements could not be performed at sufficient high Strouhal number in order to assess where resistance and reactance due to the mean flow attenuate to zero.

6.6. *Influence of edge geometry*

The influence of the edge geometry of the orifice on the impedance due to grazing flow is investigated for the 1 cm slot with turbulent boundary layer flow V. The different edge geometries are as shown in Fig. 5. The slots with asymmetrical edge geometries, Fig. 5b and c, are used with the sharp edge both upstream and downstream. Results are given in Fig. 24. The edge geometry clearly affects the amplitudes of the oscillations in resistance and reactance. Compared to the double 90° edge geometry, the geometry with the single sharp 0° edge upstream gives nearly the same results. Results for the single sharp 27° edge upstream also are very similar regarding the reactance. For the resistance a more significant difference is seen, mostly in the region around a Strouhal number of 3 where it is positive the resistance is larger. Placing the sharp edges downstream has a larger effect, especially for the 27° edge. The amplitudes of the oscillations in resistance are larger compared to both the double 90° edge geometry and the corresponding geometries with the sharp edge upstream. For the single sharp 0° edge downstream the reactance in the region where it is positive increases, for the 27° edge also a significant effect on the reactance is seen in the regions where it is negative. For the geometry with sharp 27° edges both upstream and downstream a slightly further increase is seen in the amplitude of the oscillations. In conclusion, mainly the downstream edge geometry affects the orifice impedance with grazing flow. The oscillations in non-dimensional scaled resistance and reactance are found to increase when sharp edges are used compared to the normal 90° edge geometry. The strongest effect is seen for

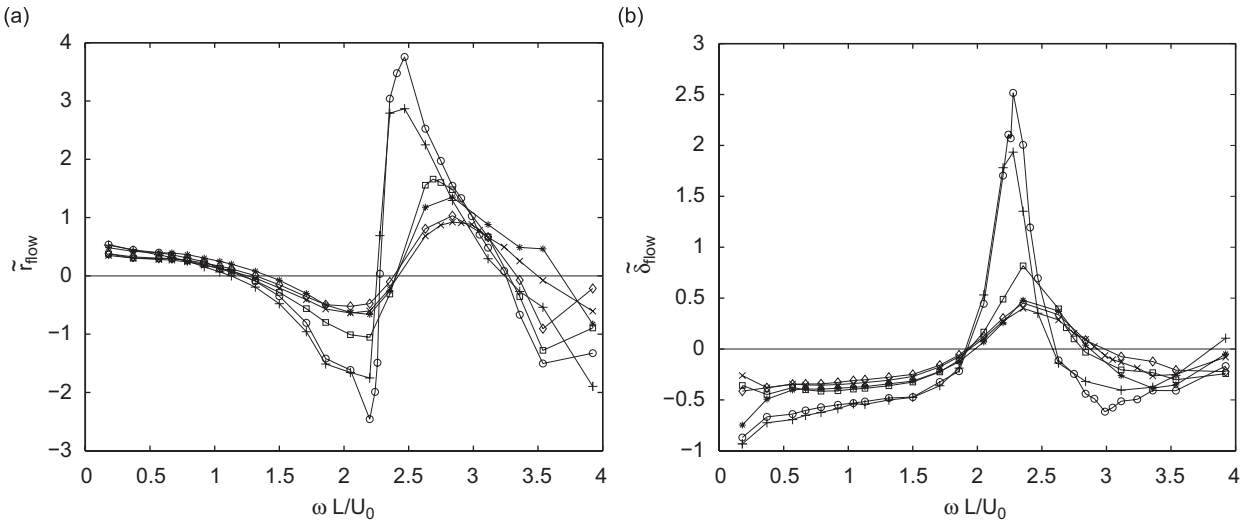

Fig. 24. Non-dimensional scaled resistance (a) and reactance (b) for the $L = 1$ orifice with different edge geometries, cf. Fig. 5, in case of boundary layer flow V. Symbols: ×, 90° edges both sides; ∗, single sharp 27° edge upstream; +, single sharp 27° edge downstream; ○, sharp 27° edges both sides; ◇, single sharp 0° edge upstream; □, single sharp 0° edge downstream.

the sharp 27° edges. This observation is in fact quite peculiar. Since the vorticity which is shed from the upstream edge plays a significant role in the interaction between sound and the grazing flow, one may expect that the upstream edge would be of most influence.

7. Conclusion

The effect of grazing mean flow on the acoustical impedance of a rectangular orifice is investigated experimentally. For this purpose an impedance tube set-up with an accurate multi-microphone technique, using lock-in signal processing, is employed.

Measurements are done for slots with different width L in the flow direction, viz. 1 and 5 cm. Furthermore, different boundary layer flows, both laminar, transitional and turbulent, are employed. In this context boundary layer characterization as well as shear layer profile measurements are carried out. Care has been taken as to remain in the regime of linear acoustic perturbations.

Both resistance and reactance due to the grazing flow display an oscillating behaviour as function of Strouhal number on the orifice width. By using the phase velocity U_c of the hydrodynamic instability, these oscillations are found at the same Strouhal numbers $\omega L/U_c$ for all configurations. On basis of the shear layer profile measurements, this convective velocity is calculated using data for the generalized hyperbolic-tangent profile provided in literature.

The presence of hydrodynamic instability, for given profile dependent on the Strouhal number $Sr_\theta = \omega\theta/U_0$ based on the shear layer momentum thickness θ and main flow velocity outside the boundary/shear layer U_0, seems to govern the presence of the oscillations in resistance and reactance. Above a critical Strouhal number the hydrodynamic instability as well as the oscillations vanish. Consequently, the ratio of slot width to momentum thickness determines the number of oscillations seen.

For boundary layers with similar shape the amplitude of the oscillations increases with decreasing boundary layer thickness (for fixed aperture width). Furthermore, the onset of nonlinearity appears to be at lower amplitudes within the regions of strong oscillations in impedance versus Strouhal number.

The influence of the edge geometry has been investigated for the 1 cm wide slot. The amplitudes of the oscillations in resistance and reactance due to the grazing flow were observed to be larger for sharp edge geometries. Especially, the form of the downstream edge—rather than the upstream edge, as one might expect—is important.

These effects of the boundary layer profile and of the orifice edge geometry are not included in existing theoretical models such as that for an infinitely thin shear layer proposed by Howe [15].

Acknowledgements

The authors would like to thank Jan Willems and Freek van Uittert. This research was financially supported by the Dutch Technology Foundation STW, grant ESF. 5645.

References

[1] R.E. Motsinger, R.E. Kraft, Design and performance of duct acoustic treatment, in: H.H. Hubbard (Ed.), *Aeroacoustics of Flight Vehicles, Theory and Practice, Vol. 2: Noise Control*, Acoustical Society of America, 1995 ISBN 1-56396-406-6.

[2] A.L. Goldman, R.L. Panton, Measurement of the acoustic impedance of an orifice under a turbulent boundary layer, *Journal of the Acoustical Society of America* 60 (6) (1976) 1397–1404.

[3] J.W. Kooi, S.L. Sarin, An experimental study of the acoustic impedance of helmholtz resonator arrays under a turbulent boundary layer, *AIAA paper 81-1998* (1981).

[4] A. Goldman, C.H. Chung, Impedance of an orifice under a turbulent boundary layer with pressure gradient, *Journal of the Acoustical Society of America* 71 (3) (1982) 573–579.

[5] A. Cummings, The effect of grazing turbulent pipe-flow on the impedance of an orifice, *Acustica* 61 (1986) 233–242.

[6] R. Kirby, A. Cummings, The impedance of perforated plates subjected to grazing gas flow and backed by porous media, *Journal of Sound and Vibration* 217 (4) (1998) 619–636.

[7] N.S. Dickey, A. Selamet, An experimental study of the impedance of perforated plates with grazing flow, *Journal of the Acoustical Society of America* 110 (5) (2001) 2360–2370.

[8] C. Malmary, S. Carbonne, Acoustic impedance measurement with grazing flow, *AIAA paper 2001-2193* (2001).
[9] Seong-Hyun Lee, Jeong-Guon Ih, Empirical model of the acoustic impedance of a circular orifice in grazing flow, *Journal of the Acoustical Society of America* 114 (1) (2003) 98–113.
[10] M. Leroux, Propagation Acoustique en Conduit Traité: Influence de l'Écoulement sur la Propagation Avec Impédance de Paroi, PhD Thesis, l'Université du Maine, Le Mans, France, 2005.
[11] G. Kooijman, Y. Aurégan, A. Hirschberg, Orifice impedance under grazing flow: modal expansion approach, *Proceedings of the 11th AIAA/CEAS Aeroacoustics Conference, AIAA paper 2005-2857* (2005).
[12] D. Ronneberger, The acoustical impedance of holes in the wall of flow ducts, *Journal of Sound and Vibration* 24 (1) (1972) 133–150.
[13] D. Ronneberger, The dynamics of shearing flow over a cavity—a visual study related to th acoustic impedance of small orifices, *Journal of Sound and Vibration* 71 (4) (1980) 565–581.
[14] J. Golliard, Noise of Helmholtz-resonator Like Cavities Excited by a Low Mach-number Turbulent Flow, PhD Thesis, l'Université de Poitiers, Fr, 2002; ISBN 90-6743-964-9.
[15] M.S. Howe, *Acoustics of Fluid– Structure Interactions*, Cambridge University Press, Cambridge, 1998 ISBN 0-521-63320-6.
[16] G. Kooijman, J. Golliard, A. Hirschberg, Orifice impedance under grazing flow measured with a single microphone method, *10th AIAA/CEAS Aeroacoustics Conference AIAA 2004-2846* (2004).
[17] K.S. Peat, Jeong-Guon Ih, Seong-Hyun Lee, The acoustic impedance of a circular orifice in grazing mean flow: comparison with theory, *Journal of the Acoustical Society of America* 114 (6) (2003) 3076–3086.
[18] X. Jing, X. Sun, J. Wu, K. Meng, Effect of grazing flow on the acoustic impedance of an orifice, *AIAA Journal* 39 (8) (2001) 1478–1484.
[19] U. Ingard, V.K. Singal, Upstream and downstream sound propagation into a moving fluid, *Journal of the Acoustical Society of America* 54 (5) (1973) 1343–1346.
[20] H. Bodén, M. Åbom, Influence of errors on the two-microphone method for measuring acoustic properties in ducts, *Journal of the Acoustical Society of America* 79 (2) (1986) 541–549.
[21] M. Åbom, H. Bodén, Error analysis of two-microphone measurements in ducts with sflow, *Journal of the Acoustical Society of America* 83 (1988) 2429–2438.
[22] W.T. Chu, Further experimental studies on the transfer-function technique for impedance tube measurements, *Journal of the Acoustical Society of America* 83 (1988) 2255–2260.
[23] P. Banks-Lee, H. Peng, Length error analysis for impedance tube measurements, *Journal of the Acoustical Society of America* 85 (4) (1989) 1769–1772.
[24] M.C.A.M. Peters, A. Hirschberg, A.J. Reijnen, A.P.J. Wijnands, Damping and reflection coefficient measurements for an open pipe at low Mach and low Helmholtz numbers, *Journal of Fluid Mechanics* 256 (1993) 499–534.
[25] A.D. Pierce, *Acoustics, an Introduction to its Physical Principles and Applications*, McGraw-Hill, New York, 1989 ISBN 0-88318-612-8.
[26] G. Ajello, Acoustic Measurements in Pipe Systems with Flow: Design of a Flow Bench and Applications to Measurement of Discontinuities, PhD Thesis, l'Université du Maine, Le Mans, France, 1997.
[27] H. Schlichting, *Boundary Layer Theory*, seventh ed., Springer, Berlin, 1979 ISBN 0-07-055334-3.
[28] J.O. Hinze, *Turbulence*, second ed., McGraw-Hill, New York, 1975 ISBN 0-07-029037-7.
[29] A. Michalke, On spatially growing disturbances in an inviscid shear layer, *Journal of Fluid Mechanics* 23 (3) (1965) 521–544.
[30] A. Michalke, The influence of the vorticity distribution on the inviscid instability of a free shear layer, *Fluid Dynamics Transactions* 4 (1969) 751–760.